Ultrafast Laser Technology and Spectroscopy

Gavin D. Reid and Klaas Wynne

in
Encyclopedia of Analytical Chemistry
R.A. Meyers (Ed.)
pp. 13644–13670

Ultrafast Laser Technology and Spectroscopy

Gavin D. Reid
University of Leeds, Leeds, UK

Klaas Wynne
University of Strathclyde, Glasgow, UK

Ultrafast laser technology and spectroscopy involves the use of femtosecond (10^{-15} s) laser and other (particle) sources to study the properties of matter. The extremely short pulse duration allows one to create, detect and study very short-lived transient chemical reaction intermediates and transition states. Ultrafast lasers can also be used to produce laser pulses with enormous peak powers and power densities. This leads to applications such as laser machining and ablation, generation of electromagnetic radiation at unusual wavelengths (such as millimeter waves and X-rays), and multiphoton imaging. The difficulty in applying femtosecond laser pulses is that the broad frequency spectrum can lead to temporal broadening of the pulse on propagation through the experimental set-up. In this article, we describe the generation and amplification of femtosecond laser pulses and the various techniques that have been developed to characterize and manipulate the pulses.

1 INTRODUCTION

Ultrafast spectroscopy has become one of the most active areas of physical chemistry. Rather than postulating mechanisms for chemical and biological reactions, ultrashort laser pulses can now be used to observe and even control the outcome of reactions in real time. Because of our improved understanding of reaction pathways, the ''arrows'' describing purported electronic motion in mechanistic organic chemistry are no longer sufficient.[1] A state-of-the-art laser system can generate 1-J ca. 20-fs pulses and the peak fluence at the focus of these lasers can exceed 10^{20} W cm^{-2}. In contrast, the total solar flux at the Earth is only 10^{17} W. An exciting new era is beginning, which will allow the possibility of using these intense ultrashort laser pulses as sources of short X-ray and electron pulses. These will reveal the positions of atoms as a function of time as reactants proceed to products through the transition states. More routinely, femtosecond lasers can be used to detect and monitor transient chemical species in solution or the gas phase, to image living cells with micrometer resolution, for laser ablation mass spectrometry (MS) and micromachining applications, which will all be of immediate interest to the analytical chemist.

With the invention of flash photolysis in 1950,[2] radical intermediates were observed by light absorption (rather than fluorescence) during the progress of a chemical reaction. When the pulsed laser followed, nanosecond experiments derived from the flash-photolysis technique were to reveal the chemistry of singlet states in solution. However, it was not until the mode-locked ruby[3] and Nd : glass[4] lasers were built in the mid-1960s that the picosecond timescale became accessible and the field of ''picosecond phenomena'' was born. When excited-state processes were studied in the picosecond domain, such as energy redistribution in molecules and proteins, proton and electron transfer reactions, photoisomerization and dissociation, and relaxation in semiconductors, many

Encyclopedia of Analytical Chemistry
R.A. Meyers (Ed.)

measured rate constants were found to be instrument limited. Nevertheless, important results such as the observation of the ''inverted region'' in electron transfer reactions[5–7] and Kramers' turnover in excited-state reactions in solution.[8,9]

However, ultrafast spectroscopy was revolutionized in the 1980s by the invention of the colliding-pulse mode-locked (CPM) dye laser, which generated 100-fs pulses in its early form[10] and 30-fs pulses as the technology was perfected.[11] This ring laser, operating at about 620 nm, coupled with improvements in dye–amplifier chains,[12] allowed the exciting field of femtochemistry to be developed,[13] which will be discussed briefly in section 5.1, and the generation of 6-fs probe pulses,[14] a record which stood until very recently. Self mode-locking in Ti : sapphire-based lasers was discovered[15] in 1990 and the early 1990s brought a new revolution – simplicity of use – and, with it, the commercialization of ultrashort pulse technology. Ti : sapphire oscillators now produce 10–20-fs pulses routinely and 4–5-fs pulses in optimized configurations using mirrors designed to reverse the ''chirp'' introduced by the Ti : sapphire rod. The limiting factor on the exceptional stability of these oscillators is the pump source and here diode-pumped solid-state laser sources are rapidly replacing large, expensive, low-efficiency ion lasers.

In parallel with improvements in oscillator technology, the technique of chirped pulse amplification[16] using solid-state gain media in regenerative or multi-pass schemes has replaced the dye–chain amplifiers of the past. A typical amplifier for routine chemistry applications produces 1 mJ per pulse at a 1-kHz repetition rate or 100 mJ at 10–20 Hz with a duration between 20 and 100 fs. Moreover, a Ti : sapphire laser oscillator and amplifier combination can be purchased in a single box less than 1 m square, operating at mains voltages with no external water-cooling requirements. Total hands-off operation is a reality and, in fact, the complete laser system can be computer controlled.

In the next section, we shall describe the technology behind Ti : sapphire lasers and amplifiers and discuss how light at almost any frequency from X-rays to terahertz can be generated and employed by the chemist. A history of the field can be found in the papers submitted to the biennial conference 'Ultrafast Phenomena', the proceedings of which are published in the *Springer Series in Chemical Physics*, which is now in its eleventh volume.[17]

2 ULTRAFAST LASERS AND AMPLIFIERS

2.1 Oscillators

Ultrashort pulses are generated by mode-locked lasers. By constructive interference, a short pulse is formed when many longitudinal modes are held in phase in a laser resonator. Various techniques have been employed, usually grouped under the terms ''active'' or ''passive'' mode locking and descriptions of these can be found in many standard texts[18,19] and review articles.[20] Active mode locking uses a modulator in the laser cavity whereas passive schemes use a saturable absorber, often a thin semiconductor film, to lock the relative phases. Modern solid-state mode-locked lasers use a different scheme called self-mode-locking and titanium-doped sapphire (Ti : sapphire) has become by far the most common laser material for the generation of ultrashort pulses. Developed in the mid-1980s,[21] Ti : sapphire has a gain bandwidth from 700 to 1100 nm peaking around 800 nm, the broadest of the solid-state materials yet discovered, high-gain cross-section and extremely good thermal conductivity. Mode locking is achieved through the action of an instantaneous nonlinear Kerr lens in the laser rod (see section 3.1). The peak fluence of the laser approaches 10^{11} W cm^{-2}, which is enough to focus the beam as it travels through the gain medium on each pass. This Kerr lens then couples the spatial and temporal modes and maintains phase locking.

A basic oscillator–cavity configuration[22] is shown schematically in Figure 1. The laser is pumped by about 5 W from a continuous wave (CW) laser source, usually now an intracavity-doubled diode-pumped neodymium laser. This light is focused into the Ti : sapphire rod, collinearly with the laser axis, through the back of one of the mirrors. The cavity consists of a Brewster-angle cut Ti : sapphire rod, 5 mm or less in length, doped to absorb about 90% of the incident pump radiation, two concave focusing mirrors placed around it, a high reflector and an output coupler. A pair of Brewster-cut fused-silica prisms are inserted to control the spectral dispersion (chirp) introduced in the laser rod. Dispersion arises from the variation of the refractive index of the material across the gain bandwidth of the laser, which can lead to a temporal separation of the resonant wavelengths and

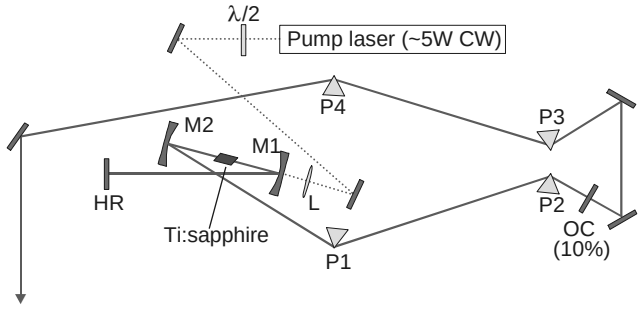

Figure 1 Diagram of a basic self-mode-locked Ti : sapphire oscillator showing the cavity layout. The pulse is coupled out from the dispersed end of the cavity, which requires a pair of matching extracavity prisms.

place a limit on the generated bandwidth (see section 2.2). The cavity dispersion, coupled to the Kerr lens effect, is an intrinsic part of the pulse-formation process. Ordinarily, the Kerr lens in the rod would contribute to the overall loss but this is overcome by a small adjustment to the resonator. Displacement of one of the curved mirrors by only ca. 0.5 mm pushes the cavity into pulsed mode. Here the cavity is corrected for the nonlinear lens effect and CW operation is restricted. Pulsing is established by perturbing the cavity to introduce a noise spike, literally by tapping a mirror mount. This configuration delivers 12-fs pulses centered at 800 nm with 5 nJ energy at an 80-MHz repetition rate. Using a shorter rod, shorter pulses have been obtained[23] as the dispersion is better compensated and space–time focusing effects are controlled. The laser repetition rate can be adjusted by the insertion of a cavity dumper in a second fold, without prejudice to the pulse duration.[24] The use of mirrors that have dispersion opposite to that of the rod[25] obviates the need for prisms entirely. Alternatively, a mixture of prisms and mirrors can be used to generate pulses as short as 5 fs.[26] At the time of writing, the use of mirrors with well-defined chirp characteristics is complicated by the demand for extreme tolerances in the manufacturing process. Many schemes have been proposed for self-starting oscillators, perhaps the best of which is the use of a broadband semiconductor saturable-absorber mirror in the cavity.[27] Advances in these areas will surely continue.

Other important solid-state materials include Cr : Li-SAF (chromium-doped lithium–strontium–aluminum fluoride), which can be pumped by red diode lasers and operates close to the peak Ti : sapphire wavelength, and Cr^{4+} : YAG, which lasers at around 1.5 μm, an important communication wavelength. Cr : forsterite lases, operating at about 1.2 μm, can be frequency doubled to the visible region and have been used for imaging applications (see section 5.2). Furthermore, passively mode-locked frequency-doubled erbium-doped fiber lasers have been developed commercially. These lasers operate between 1530 and 1610 nm and efficient frequency doubling to 765–805 nm is possible in periodically poled nonlinear crystals (i.e. these lasers can be used in place of Ti : sapphire for many applications).[28] They have the advantage of being cheap and extremely compact since they do not require complicated dispersion-compensation schemes, owing to the soliton nature of the pulses supported in the fiber. They can also be pumped using cheap large-area telecommunications-standard laser-diode sources. Unfortunately, the pulse duration is limited to a minimum of about 100 fs.

2.2 Dispersion and Pulse Broadening

A bandwidth-limited pulse has a spectral width given by the Fourier transform of its time-domain profile.

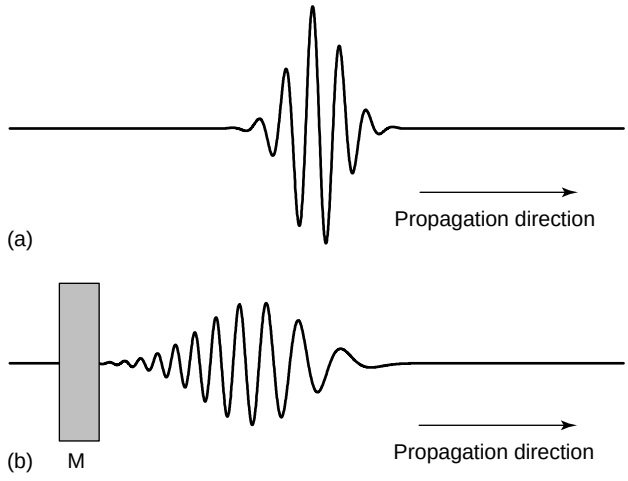

Figure 2 Schematic diagram of the electric field of (a) an undispersed Gaussian pulse and (b) the same pulse after traveling through a positively dispersing medium, M. A frequency sweep from low to high frequency (right to left) can be observed on the trace in (b).

Consequently, a 10-fs full width at half-maximum (fwhm) Gaussian pulse centered at 800 nm has a bandwidth of 94 nm (1466 cm^{-1}). When a short pulse travels through a dispersive medium, the component frequencies are separated in time. Figure 2(a) and (b) shows the effect of dispersion on a Gaussian pulse traveling through a piece of glass. There are two points to note. First, the center of the pulse is delayed with respect to a pulse traveling in air. This is usually called the group delay, which is not a broadening effect. Second, normally dispersive media such as glass impose a positive frequency sweep or "chirp" on the pulse, meaning that the blue components are delayed with respect to the red.

In order to get a physical feel for the effect of the chirp, it is common to consider the phase shift as a function of frequency w. The phase, $\varphi(w)$ can be developed as a power series about the central frequency w_0, assuming the phase varies only slowly with frequency according to Equation (1):

$$\varphi(w) = \varphi(w_0) + (w - w_0)\varphi'(w_0) + \tfrac{1}{2}(w - w_0)^2\varphi''(w_0) + \tfrac{1}{6}(w - w_0)^3\varphi'''(w_0) + \tfrac{1}{24}(w - w_0)^4\varphi''''(w_0) + \cdots \quad (1)$$

where (Equation 2):

$$\varphi'(w_0) = \left.\frac{\partial\varphi}{\partial\varphi}\right|_{w=w_0}, \varphi''(w_0) = \left.\frac{\partial^2\varphi}{\partial w^2}\right|_{w=w_0},$$
$$\varphi'''(w_0) = \left.\frac{\delta^3\varphi}{\delta w^3}\right|_{w=w_0}, \text{etc.} \quad (2)$$

φ' is the group delay, φ'' the group delay dispersion (GDD) [or group velocity dispersion (GVD)] and φ'''

and φ'''' are simply the third-order dispersion (TOD) and fourth-order dispersion (FOD).

For the sake of simplicity, consider a transform-limited Gaussian pulse with a central frequency w_0 and a pulse width (fwhm) τ_{in}. Then its electric field, E_{in}, takes the form (Equation 3)

$$E_{in}(t) = E_0 \exp\left[-\left(\frac{2\ln 2t^2}{{\tau_{in}}^2}\right) + iw_0t\right] \qquad (3)$$

The electric field after traveling through a dispersive medium can be found by transforming E_{in} to the frequency domain and adding the components from the phase expansion $\varphi(w)$ in Equation (1) before transforming back. If we assume only a contribution from the GDD term, the electric field E_{out} is given by Equation (4):[18]

$$E_{out}(t) = E_0 \exp\left[i(w_0t - \varphi) - \Gamma(t - \varphi')^2\right] \qquad (4)$$

where (Equation 5)

$$\Gamma = \left(\frac{\tau_{in}^2}{2\ln 2} + 2i\varphi''\right)^{-1} \qquad (5)$$

The effects of this dispersion are twofold. First, by inspection of the Gaussian part of E_{out}, τ_{out} is analogous to τ_{in} from E_{in} and is broadened with respect to the input-pulse width by a factor (Equation 6)

$$\frac{\tau_{out}}{\tau_{in}} = \sqrt{1 + \frac{\varphi''^2}{\tau_{in}^4}16(\ln 2)^2} \qquad (6)$$

Second, a frequency sweep is introduced in the output pulse (because the expression in Equation (5) is complex) with a sign that is opposite to that of φ''.

The GDD, φ''_m, due to material of length l_m, is related to the refractive index of the material, $n(\lambda)$, at the central wavelength, λ_0, through its second derivative with respect to wavelength (Equation 7):

$$\varphi''_m = \frac{\lambda_0^3 l_m}{2\pi c^2}\frac{d^2 n(\lambda)}{d\lambda^2} \qquad (7)$$

Figure 3(a) shows the variation of refractive index with wavelength for some common materials and Figure 3(b) shown the GDD. The data were obtained from glass suppliers and the fits are to Sellmeier-type equations, which are then used to take the numerical derivatives for use in subsequent calculations.

Using Equations (6) and (7) together with refractive index data, we can calculate values for the GDD arising from a length of material. Figure 4 shows the effect of 10 mm of fused silica on a short pulse. Silica is one of the least dispersive materials available and 10 mm is chosen to represent one or two optical components, which might be part of an experimental arrangement. If we consider a pulse of around 100 fs in duration, the effect is minimal but visible. However, a 10-fs pulse is broadened by more than a factor of 10!

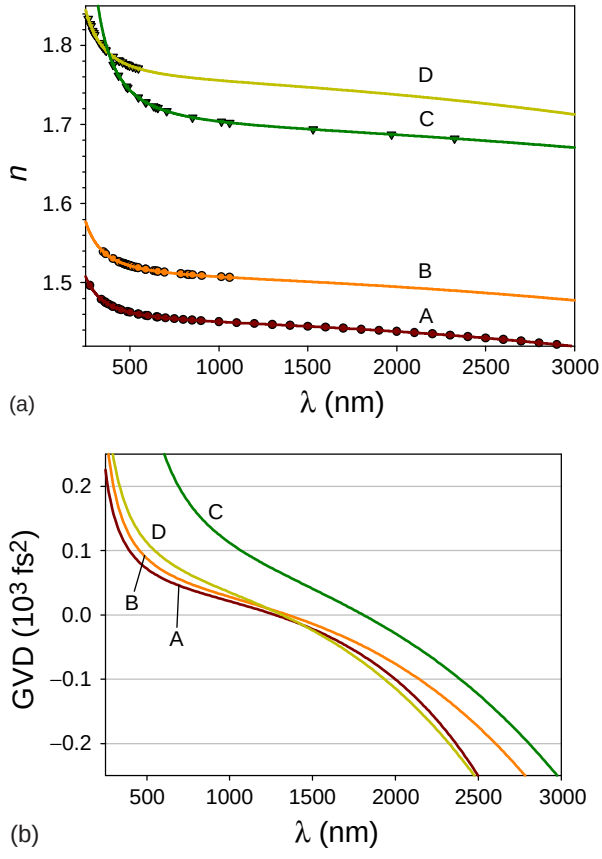

Figure 3 (a) Refractive index versus wavelength data for some common materials: (A) fused silica, (B) Schott BK7, (C) Schott SF10 and (D) sapphire. The points are measured values and the lines are fits to Sellmeier equations. (b) The GDD for 1 mm of material derived from the fits.

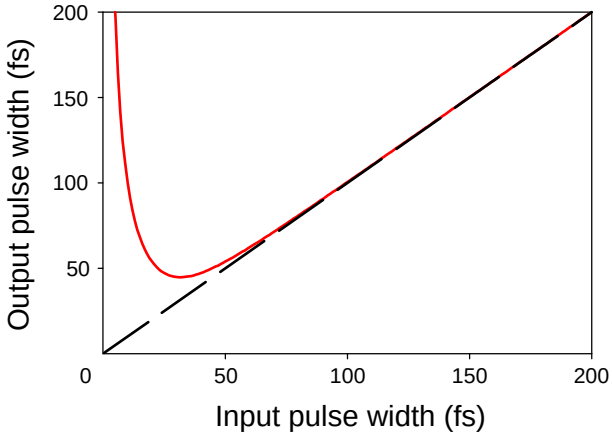

Figure 4 Gaussian pulse width before and after 10 mm of fused silica (solid line), corresponding to one or two optical components. The broadening is due to GDD.

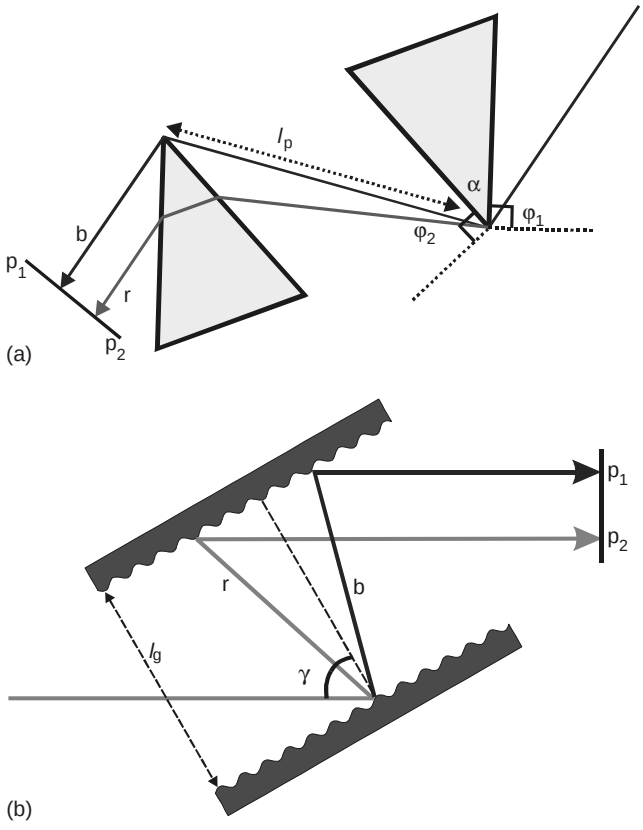

Figure 5 (a) Prism and (b) grating pairs used in the control of dispersion; r and b indicate the relative paths of arbitrary long- and short-wavelength rays. φ_1 is the (Brewster) angle of incidence at the prism face. The light is reflected in the plane $p_1 - p_2$ in order to remove the spatial dispersion shown.

A good understanding of dispersion is essential in order to deliver a short pulse to the sample and careful control of the phase shift is necessary. Fortunately, a number of designs using prism and grating pairs have been devised whereby this can be achieved.[29] The two most important schemes are shown in Figure 5(a) and (b). The Ti : sapphire oscillator we discussed above uses the prism pair.[30] This arrangement creates a longer path through the prism material for the red wavelengths compared with the blue, introducing a negative dispersion. Provided that the prism separation, l_p (defined tip to tip), is sufficiently large, the positive dispersion of the material can be balanced. The prism apex angle is cut such that at minimum deviation of the center wavelength, the angle of incidence is the Brewster angle. Here, the Fresnel reflection losses for the correct linear polarization are minimized and the system is essentially loss free. The second scheme is the parallel-grating pair[31] and, again, a longer path is created for the red over the blue. Grating pairs (Figure 6) introduce negative GDD at very modest separation leading to compact designs but suffer from losses of close to 50% in total. Both prism and grating

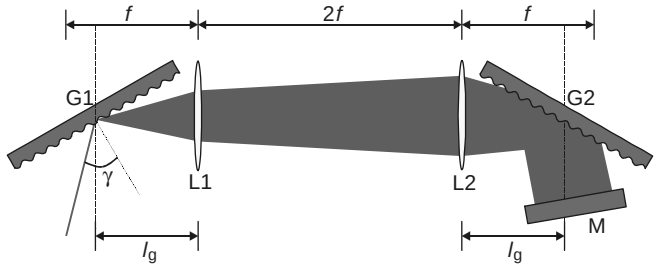

Figure 6 Schematic diagram of a grating-pair pulse stretcher showing the arrangement for positive dispersion. G1 and G2 are diffraction gratings, L1 and L2 are identical lenses separated by twice their focal length, f, and M is a mirror acting to double-pass the beam through the system. The distance $l_g - f$ determines the total dispersion.

pairs are used in a double-pass arrangement to remove the spatial dispersion shown in the diagram.

Expressions for calculating the dispersion are given in Table 1. The equations look a little daunting but the dispersion can be modeled easily on a personal computer. To illustrate this point, Figure 7 shows the total GDD and TOD arising from 4.75 mm of sapphire balanced against a silica prism pair separated by 60 cm. This is typical of a Ti : sapphire oscillator. The net GDD is nearly zero at 800 nm but the net TOD remains negative at the same wavelength. In fact, it is a general observation that prism compressors overcompensate the third-order term. The greater the dispersion of the glass, the less distance is required, but the contribution of the third-order term increases. Experimentally, there must usually be a compromise between prism separation and material.

Grating pairs are important in amplification and will be considered in more detail below. Significantly, however, the sign of the third-order contribution from the grating pair is opposite to that of the prisms, allowing a combined approach to dispersion compensation, which has been used to compress pulses in the 5-fs regime.[14] It can be more useful to think in terms of the total GDD versus wavelength with a view to keeping the curve as flat and as close to zero as possible across the full bandwidth of the pulse.

Mirror coatings have been developed which can provide second- and third-order compensation. This so-called ''chirped'' mirror reflects each wavelength from a different depth through the dielectric coating, which is made up of multiple stacks of varying thickness. In combination with a prism pair, this technique has been as successful as the grating/prism combination without the associated losses. This type of system will become more common as the mirrors, tailored to individual requirements, become available commercially.

Table 1 Expressions (Equations 8–17) for the dispersion for material, prism and grating pairs

The accumulated phase in a double-pass *prism compressor* (see Figure 5a) is

$$\varphi(w) = \frac{2wl_p}{c}\cos\left(\varphi_2^{\text{bluest}} - \varphi_2\right) \tag{8}$$

where φ_2 is the (frequency-dependent) exit angle, $\varphi_2^{\text{bluest}} = \varphi_2(w_{\text{bluest}})$ is the exit angle of the shortest-wavelength light transmitted by the prism pair:

$$\varphi_2(w) = \arcsin\{n\sin[\alpha - \arcsin(n^{-1}\sin\varphi_1)]\} \tag{9}$$

where n is the (frequency-dependent) refractive index of the prism material, φ_1 is the (frequency-independent) angle of incidence on the first prism and α is the prism top angle. If the prism compressor is designed for frequency w_{design}:

$$\alpha = 2\arcsin\left(\frac{1}{\sqrt{1+n_{\text{design}}^2}}\right) \tag{10}$$

$$\varphi_1 = \arcsin\left[n_{\text{design}}\sin\left(\frac{\alpha}{2}\right)\right] \tag{11}$$

where n_{design} is the refractive index of the prism at the design wavelength. Expressions for the group delay, GVD, TOD and FOD can be obtained by taking derivatives of Equation (8).

The group delay in a *grating compressor/stretcher* (see Figures 5b and 6) is

$$\frac{d\varphi}{dw} = \frac{P}{c} \tag{12}$$

where the optical pathlength is

$$P = L\frac{1+\cos\theta}{\cos(\gamma-\theta)} \tag{13}$$

$$\theta(w) = \gamma - \arcsin\left(\frac{2\pi c}{wd} - \sin\gamma\right) \tag{14}$$

with γ the angle of incidence on the first grating and d the groove frequency. In the case of a grating *compressor*, $L = l_g$. In the case of a grating *stretcher*, $L = 2(l_g - f)\cos\gamma$.

Expressions for the GVD, TOD and FOD can be obtained by taking derivatives of Equation (12). For a double-pass grating compressor/stretcher, the analytical expression

$$\frac{d^2\varphi}{dw^2} = \frac{-\lambda^3 L}{\pi c^2 d^2}\left[1 - \left(\frac{\lambda}{d} - \sin\gamma\right)^2\right]^{-3/2} \tag{15}$$

is found, where λ is the wavelength.

The accumulated phase in *material* is

$$\varphi(w) = \frac{wnl_m}{c} \tag{16}$$

where l_m is the length of the material. Expressions for the group delay, GVD, TOD and FOD can be obtained by taking derivatives of Equation (16). An analytical expression for the GVD is

$$\frac{d^2\varphi}{dw^2} = \frac{\lambda^3 l_m}{2\pi c^2}\frac{d^2n}{d\lambda^2} \tag{17}$$

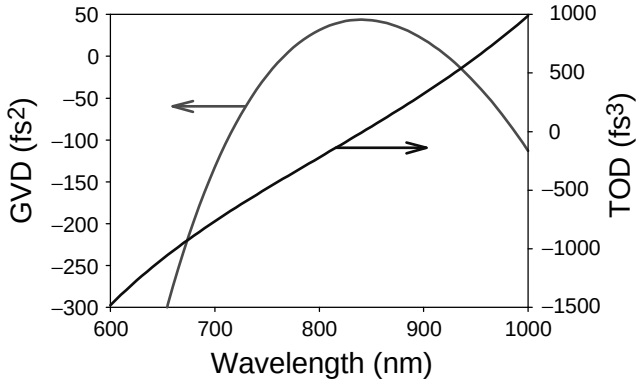

Figure 7 The residual GVD and TOD arising from the balance between the dispersion of a 4.75-mm Ti : sapphire laser rod and the intracavity silica prism pair separated by 60 cm.

2.3 Chirped-pulse Amplification

The amplification of nanojoule-level femtosecond pulses to the millijoule level and above is complicated by the extremely high peak powers involved. A 1-mJ 20-fs pulse focused to a 100-μm spot size has a peak fluence of $5 \times 10^{12}\,\text{W cm}^{-2}$. The damage threshold of most optical materials is only a few gigawatts per square centimeter, 1000 times lower. The problem is overcome by stretching the pulse in time using dispersion to advantage. This is followed by amplification and subsequent recompression to the original pulse duration. This technique also has the benefit of eliminating unwanted nonlinear effects in the amplifier materials. A diagram showing the principle of chirped-pulse amplification (CPA) is shown in Figure 8.

The pulse stretcher is a variation of the grating pair described above.[32] A unity-magnification telescope is placed between two gratings in an antiparallel rather than parallel geometry. This reverses the sign of the dispersion

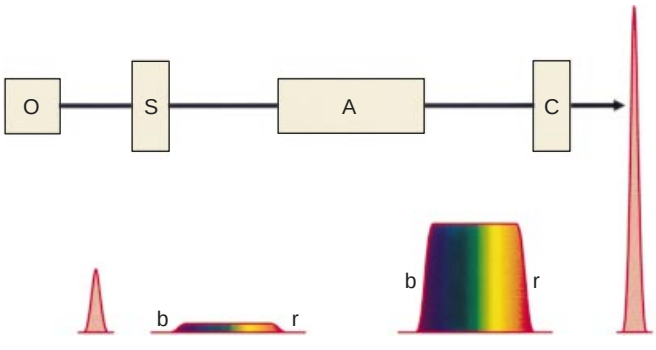

Figure 8 Diagram showing the principle of CPA. The oscillator output (O) is stretched in the grating stretcher (S) such that the red frequency components (r) travel ahead of the blue (b). The peak intensity is reduced in the process. The stretched pulse is then amplified in a regenerative or multipass amplifier (A) before recompression in a grating-pair compressor (C).

of the grating pair but otherwise the mathematical expressions given in Table 1 are identical.

The stretching factor is defined by the effective grating separation $L = 2(l_g - f)$, where f is the focal length of the lens and l_g the distance from the lens to the grating. Typically, the pulse duration is increased to 100 ps or more for efficient extraction of the stored energy. When l_g is equal to f, there is no dispersion, and when l_g becomes larger than f, the dispersion changes sign. In practice, the lenses are replaced by a single spherical or parabolic mirror in a folded geometry, which eliminates chromatic aberration and allows gold-coated holographic gratings to be used near their most efficient Littrow angle of incidence, $\arcsin(\lambda_c/2d)$, where λ_c is the central wavelength and d the line separation of the grating. Other more sophisticated stretcher designs, one for example based on an Offner triplet,[33] have been made but are outside the scope of this discussion. Ignoring the amplifier for now, the pulse is recompressed using an identical parallel grating pair separated by $2l_g$.

CPA technology developed rapidly during the 1990s. Solid-state materials usually have long upper-state radiative lifetimes compared with laser dyes. The large saturation fluence (1 J cm^{-2}) and long storage time (3 μs) of Ti : sapphire make it an ideal amplifier gain material. Here we shall consider two basic schemes, the regenerative and the multipass amplifier. These operate either at 10–20 Hz, pumped by a standard Q-switched Nd : YAG laser giving up to 100 mJ at 532 nm, or at 1–5 kHz pumped by an intracavity-doubled acousto-optically modulated CW Nd : YLF laser, which usually provide more than 10 W at 527 nm in a 200-ns pulse. These pump lasers are normally flash-lamp pumped but diode-pumped equivalents have appeared commercially in recent months. A good spatial mode quality is essential and a clean top-hat profile is ideal.

Figure 9(a) and (b) shows two arrangements for regenerative amplification. The arrangement in Figure 9(a) is often used at 1 kHz.[34] Briefly, a single vertically polarized pulse from the oscillator, stretched to ~100 ps, is injected into the amplifier using a fast-switching PC. This is performed by stepping the voltage in two stages, first by a quarter wave, in order to trap the pulse in the amplifier cavity, and then up to a half wave for ejection. Typically, the pulse makes around 12 round trips in the cavity before the gain is saturated. A FR is used to isolate the output pulse from the input. The arrangement in Figure 9(b)[35] differs in two respects. First, the focusing in the cavity is relaxed in order to remain near the saturation fluence for the more energetic pulses at 10 Hz. Second, the PC is used to switch the pulse in and out while it is traveling in opposite directions. This has two great advantages for short pulses: (1) there is only one pass made through the Faraday isolator, which has extremely large dispersion and only a limited spectral bandwidth, and (2) it is only necessary to apply a half-wave voltage to the PC at the moment the pulse is switched in or out of the cavity. Again, this is to avoid bandwidth-limiting effects.

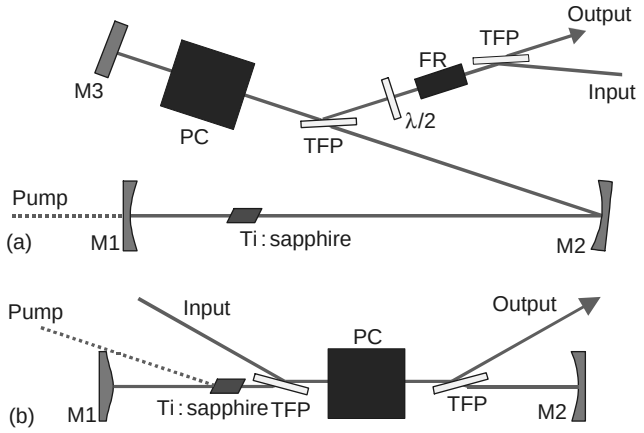

Figure 9 Two schemes for regenerative amplification. The design in (a) is often used for kilohertz repetition rate amplifiers and that in (b) at a 10–20-Hz repetition rate. The Ti : sapphire rod is usually ca. 20 mm long and doped for 90% absorption. TFP, thin-film polarizing beamsplitter; PC, Pockels cell; FR, Faraday rotator; λ/2, half-wave plate. In (a), M1 is 150 mm radius of curvature, M2 is 1 m and M3 is flat. In (b) M1 is −20 m and M2 is +10 m.

An alternative and perhaps more straightforward design for amplification of femtosecond pulses is based on the multipass scheme that has been used in the past with dye amplifiers. One of the best arrangements for use at kilohertz repetition rates[36] is shown in Figure 10 and an example of a 10-Hz system can be found in a paper by Chambaret et al.[37] A PC is used to inject a single pulse from the 80-MHz pulse train into the amplifier, where it is allowed to make about eight passes with a slight offset at each cycle before being picked off and ejected. The

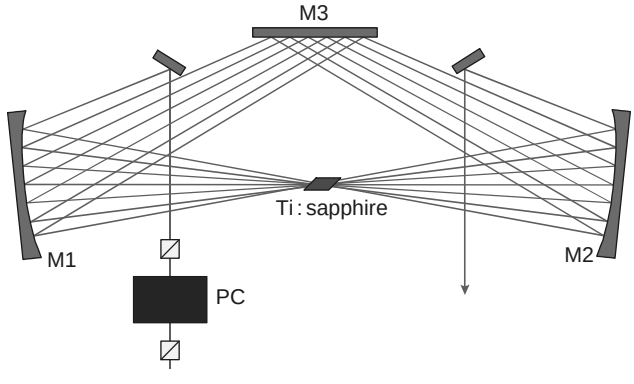

Figure 10 Multipass-amplifier arrangement. M1, M2 are 1-m radius of curvature mirrors and M3 is flat and up to 15 cm wide. A PC and a pair of polarizers are used to inject a single pulse into the amplifier.

pulse incurs significantly less loss in these arrangements, accrues much less chirp and only one pass is made through the PC. There is also no need for a Faraday isolator.

Additional power-amplification stages may be added to increase the pulse energy further. The ring configuration can be modified by arranging for the beams to cross away from the focus to achieve a different saturation fluence. In this configuration, 4 W after recompression at 1 kHz has been obtained.[38] At kilohertz repetition rates, the presence of a thermally induced refractive index change across the spatial profile of the beam must be avoided in order to achieve diffraction-limited output. This is achieved either by cooling to 120 K where the thermal properties of sapphire are much improved[39] or by using the lens to advantage.[40] At lower repetition rates, the medium has time to recover and a thermal lens is usually not established. In this regime, power amplifiers can be added to the limit of available pump energy. An additional complication requires that short pulses of more than a few millijoules in energy must be recompressed under vacuum to avoid nonlinear effects and ionization of the air.

2.4 Pulse Recompression

Clearly, the amplification process introduces extra dispersion and one of the major considerations in system design is the recompression process. The naive approach is to add additional separation between the gratings in the pulse compressor and this is how the first systems were built. Unfortunately, the stretcher and compressor combination is the most dispersive part of the system and a mismatch between the two introduces vast third- and fourth-order contributions to the phase expansion. The easiest way to correct the TOD is to adjust the angle of incidence between the stretcher and compressor, which changes the third-order contribution. Figure 11 (line A) shows the net group-delay dispersion versus wavelength for the kilohertz regenerative amplifier discussed above. The GDD curve is essentially flat over only a narrow wavelength range although the GDD and TOD are zero simultaneously at the center wavelength. Table 2 shows the bandwidth (fwhm) of Gaussian pulses of different durations. Ideally, the GDD curve should be flat over perhaps twice the bandwidth to avoid phase distortions.

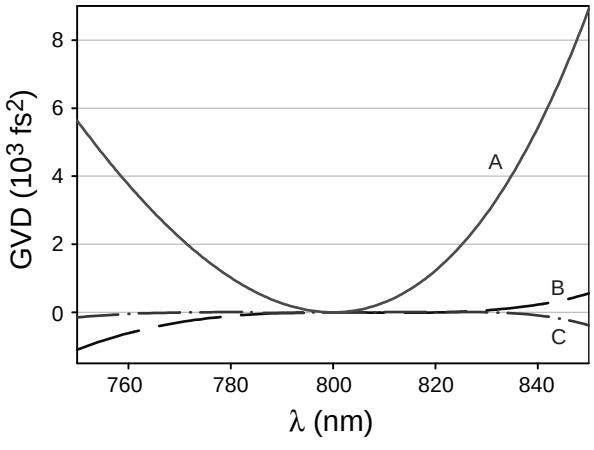

Figure 11 Solid line (A): the net GVD due to the stretcher–amplifier–compressor combination using 1200 lines mm^{-1} diffraction gratings. The difference between the angle of incidence in the stretcher compared to the compressor is 10.32° and the extra grating displacement is 69.4 mm. Dashed line (B): the same using 1200 lines mm^{-1} gratings in combination with an SF18-glass prism pair. The difference between the angle of incidence in the stretcher compared with the compressor is 3.4° and the extra grating displacement is 26.2 mm. The prism separation is 2.4 m. Dashed-dotted line (C): the same, using a 1200 lines mm^{-1} diffraction grating in the stretcher and an 1800 lines mm^{-1} grating in the compressor in combination with an SF10-glass prism pair. The angle of incidence in the stretcher is 13° and in the compressor 39°. Littrow is 41°. The prism separation is 1.65 m.

Recall that the third-order contribution from prism pairs has the opposite sign to gratings.[41] This fact can be used to null the GDD, TOD and FOD terms and this is illustrated in Figure 11 (line B). The difference is dramatic and this system will support much shorter pulses at the expense of 2.4 m of pathlength between the SF18 prism pair.

Another method in the recent literature[42] uses gratings of different groove density in the compressor compared with the stretcher balanced against additional round trips in the amplifier. This method, while better than the angular adjustment technique, is not as effective as the grating–prism combination approach, although it has found favor in commercial application owing to its inherent compactness. Typical parameters are a 1200 lines mm^{-1} grating in the stretcher at an angle of incidence of only 6° and 2000 lines mm^{-1} in the compressor at 57°, which is reasonably close to Littrow geometry (55°). Gratings with 2000 lines mm^{-1} are significantly more efficient than those with 1200 lines mm^{-1}, giving improved throughput in the compressor. However, a combination of mixed gratings and a prism pair as shown in Figure 11 (line C) is a little better than matched gratings and prisms with the benefit of extra throughput and reduced prism separation without the need to balance the

Table 2 Pulse duration versus bandwidth (fwhm) for Gaussian-shaped pulses centered at 800 nm

Gaussian pulse duration (fwhm) (fs)	Gaussian bandwidth (fwhm) (nm)
100	9.4
50	18.8
30	31.3
10	94

total dispersion with extra amplifier material.[43] This system will support 20-fs pulses with little phase distortion.

2.5 Saturation Effects

The gain cross-section, σ_g, is not constant as a function of wavelength. Since this appears as an exponent in calculating the total gain, successive passes through the amplification medium can lead to pulse spectral narrowing and a shift in the central wavelength. This limits the maximum bandwidth to 47 nm in Ti : sapphire.[38] As the gain approaches saturation, the leading red edge of the pulse extracts energy preferentially and the spectrum will red shift. The maximum gain bandwidth can be achieved by seeding to the blue of the peak, allowing the gain to shift towards the maximum on successive passes. Second, by altering the gain profile by discriminating against the peak wavelengths using an étalon or a birefringent filter, termed regenerative pulse shaping, the theoretical limit can be overcome.[44]

3 WAVELENGTH CONVERSION

Ultrafast lasers and amplifiers typically operate at a very limited range of wavelengths. For example, Ti : sapphire-based ultrafast lasers are tunable in the near-infrared (NIR) region from about 700 to 1000 nm but typically work best at about 800 nm. The high peak power of these lasers can be used, however, to convert the laser light to different wavelengths. In fact, in some cases ultrafast laser systems may be the ideal or only route to make radiation at certain wavelengths. Below, a series of techniques are described to convert femtosecond laser pulses at visible wavelengths to other wavelengths.

3.1 White-light Generation and the Optical Kerr Effect

At high intensities such as on the peak of an ultrashort laser pulse, the refractive index of any medium becomes a function of the incident intensity. This effect, which is often referred to as the optical Kerr effect (OKE),[45] can be described by Equation (18):

$$n(I) = n_0 + n_2 I + \cdots \tag{18}$$

where n_0 is the normal refractive index of the medium and n_2 is the nonlinear refractive index. The nonlinear refractive index is very small, for example, in fused silica $n_2 \approx 3 \times 10^{-16}\,\mathrm{cm^2\,W^{-1}}$. A laser pulse with center frequency w traveling through a medium of length L will acquire an optical phase wLn/c and therefore the effects of the nonlinear refractive index will become important when this phase factor becomes comparable to a wavelength. As an example, consider the propagation of femtosecond pulses through an optical fiber. With a 9-μm fiber-core diameter (typical for communications-grade fiber), 10-nJ pulse energy and 100-fs pulse width, the peak power is 100 kW, corresponding to a power density of $1.5 \times 10^{11}\,\mathrm{W\,cm^{-2}}$. If the length of the fiber is 1 cm, the optical pathlength changes by $Ln_2I = 472$ nm or half a wavelength. From this calculation, it can be seen that the OKE can have a significant effect on a femtosecond pulse traveling through a medium. For pulses with energies in the order of millijoules or higher, even the nonlinear refractive index of air becomes important.

To understand how the OKE can modify the spectral properties of an ultrashort pulse, one has to consider how the nonlinear refractive index modifies the optical phase of the pulse. The electric field of a laser pulse traveling in the x direction can be written as Equation (19):

$$E(t)\cos(wt - kx) \tag{19}$$

where $k = wn/c$ is the wavenumber. Since the wavenumber depends on the (nonlinear) refractive index of the medium, the pulse will acquire a time-dependent phase induced by the Kerr effect. Inserting Equation (18) into Equation (19) and performing a Taylor expansion around the peak of the ultrashort pulse, one finds (Equation 20)

$$E(t)\cos[(w + \xi t)t - kx] \tag{20}$$

where ξ depends on the nonlinear refractive index, the pulse width and peak power, and the distance traveled. Consequently, the nonlinear refractive index induces an approximately linear frequency sweep (or chirp, see section 2.2 and Figure 12) on the pulse. In other words, the spectrum of the pulse has broadened owing to the nonlinear interaction. If a single pulse modifies its own characteristics in this way, the effect is often referred to as self-phase modulation. If one pulse modifies the effective refractive index causing a second pulse to change its characteristics, this is referred to as cross-phase modulation.

The spectral broadening induced by the nonlinear refractive index is extremely useful in spectroscopic applications. For example, an 800-nm femtosecond pulse can be sent through a short length of fiber or through a few millimeters of glass or sapphire to produce a broadband output pulse. Often there will be significant power at wavelengths ranging from 400 nm to 1.6 μm. For this reason, such spectrally broadened pulses are referred to as white-light continuum pulses. The white-light continuum generated in a fiber has been used to generate some of the world's shortest pulses of around 5 fs.[46,47] A white-light continuum pulse is an ideal seed for an optical parametric amplifier (see section 3.3).

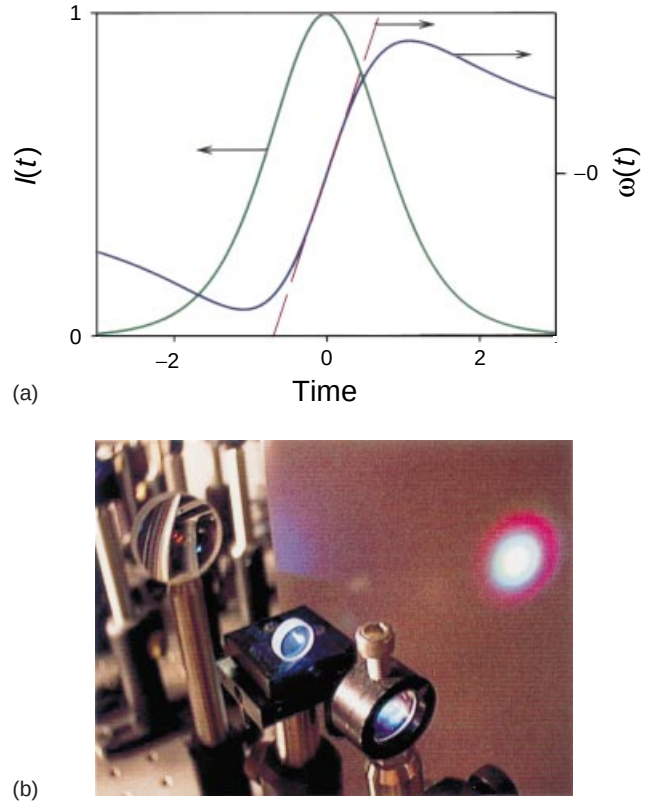

Figure 12 (a) Chirp on an ultrashort pulse induced by the nonlinear refractive index of a dielectric medium. The input pulse has a sech^2 envelope and the figure shows the instantaneous frequency within the pulse. A Taylor expansion around the peak of the pulse shows that the frequency sweep is approximately linear around time zero. (b) Photograph of a femtosecond white-light continuum beam generated in a piece of sapphire. (Picture courtesy of the Center for Ultrafast Optical Science, University of Michigan.)

An implication of the nonlinear refractive index is self-focusing or defocusing. As a laser beam is typically more intense in its center, the nonlinear change of the refractive index will be strongest in the center. As a result, the medium will act as an intensity-dependent lens. In a set-up in which the sample is translated through the focus of a beam, this effect can be used to measure the nonlinear refractive index of a sample quickly. Self-focusing is the basis of the Kerr lens mode locking (KLM) effect used in ultrashort lasers (see section 2.1). Self-focusing can become a run-away process leading to beam distortion and catastrophic damage to optical components. In white-light generation, self-focusing can result in the beam breaking up into multiple filaments that make the white-light output extremely unstable. It is therefore of the utmost importance to choose the incident power such that white light is generated without producing multiple filaments. For a 100-fs pulse, this usually means that the pulse energy should be limited to approximately 1 μJ.

3.2 Generation of Ultraviolet and X-rays

The very high peak power that can be achieved with femtosecond pulses means that in principle nonlinear frequency conversion should be very efficient. It should be straightforward to use second-harmonic generation (SHG), third-harmonic generation (THG) and fourth-harmonic generation (FHG) to produce femtosecond pulses in the near- to deep-ultraviolet (UV) region. However, the group velocity of the pulses (see section 2.2) depends on the center wavelength and changes significantly as the UV region is approached. For example, in a 1-mm β-barium borate (BBO) crystal (suitable for harmonic generation down to about 180 nm) the difference in group delay between the fundamental and the fourth harmonic is 3.3 ps (see Table 3). Depending on the set-up, this implies that the conversion efficiency is very low or the pulses produced are very long.[48] Therefore, when UV pulses are produced, it is extremely important to use the thinnest possible nonlinear crystals. As a rough guide, one should choose the thickness of the crystal such that the group-delay difference between the fundamental and the harmonic is about equal to or less than the width of the pulse. An efficient harmonic-generation set-up will also use multiple conversion steps and between steps readjust the relative time delay between the laser pulses at different wavelengths.[49]

Most nonlinear crystals used for harmonic generation [BBO, lithium triborate (LBO), potassium dihydrogen-phosphate (KDP), etc.] are opaque in the deep-UV region. Very high harmonic generation in low-pressure gases has been used successfully to generate deep-UV and soft X-ray pulses. It was recently shown[50] that a glass capillary could be used to modify the phasematching condition for coherent soft X-ray generation. Using this set-up, femtosecond pulses at 800 nm were converted to the 17–32-nm wavelength range (~30th harmonic) with about 0.2 nJ energy per harmonic order. A similar set-up was used[51] to mix 800- and 400-nm pulses to produce 8-fs pulses at 270 nm. Extremely short (5 fs) amplified laser pulses have been used[52] to generate X-rays (~4 nm) in the water window by harmonic generation in a gas jet.

Table 3 Group delays calculated from the refractive index of BBO, of femtosecond pulses at various wavelengths traveling through a 1-mm crystal (ordinary polarization)

Wavelength (nm)	τ_{group} (ps)	$\Delta\tau_{group}$ (ps)
800	5.62	–
400	5.94	0.32
267	6.74	1.12
200	8.97	3.34

The advantage of very high harmonic generation is that the X-rays are generated in a well-collimated beam. The disadvantage is that it has not yet been shown to be possible to generate hard X-rays with wavelengths smaller than a molecular bond length.

Electron impact sources could generate femtosecond hard X-rays if high-charge, high-energy femtosecond electron bunches were available. Even so, electron impact sources have the disadvantage that the X-rays are emitted in a 2π solid angle, which makes their brightness typically very low. Therefore, these sources are difficult to use in diffraction experiments although not strictly impossible. Very high-power laser pulses [peak powers of the order of 1 TW (10^{12} W)] can be used to generate laser-produced plasmas.[53] Typically, a high-power laser pulse is used to evaporate a (metal) target and produce a plasma by stripping electrons off the atoms with multiphoton ionization.[54] Recombination of these electrons with the ions results in the emission of hard X-ray pulses (wavelengths of the order of 1 Å). Very recently, it has been shown that reverse Thompson scattering of terawatt laser pulses off a high-energy (50 MeV) electron beam can be used to produce hard X-rays (0.4 Å).[55] However, only 10^4 X-ray photons were generated per laser shot, resulting in about one diffracted X-ray photon per shot in diffraction off Si ⟨111⟩.

3.3 Optical Parametric Amplifier for Infrared Generation

The infrared (IR) region of the spectrum is very important for the sensing of a great variety of (transient) molecular species. Femtosecond IR pulses can be used to determine which bonds in a molecule break or form. The mid-IR fingerprint region is ideally suited to determine the presence of specific molecules in a sample. Therefore, a great deal of effort has been invested over the last decade to produce femtosecond pulses tunable in the near- and mid-IR regions. Most techniques in use now are based on parametric difference-frequency processes (see Figure 13a and b).[56] In difference-frequency mixing, a strong femtosecond pulse at frequency $w_1 + w_2$ mixes in a nonlinear crystal with a (weaker) pulse at frequency w_1, to produce a new beam of femtosecond pulses at frequency w_2. If the incident power at frequencies w_1 and w_2 is zero, a nonlinear crystal can produce these frequencies spontaneously in a process referred to as optical parametric generation (OPG). If the incident power at frequencies w_1 and w_2 is small but nonzero, the pump pulse at frequency $w_1 + w_2$ can amplify the former frequencies in what is referred to as OPA. Since the peak power of a femtosecond pulse can be extremely high while the pulse energy is relatively low, one can produce enormous parametric gain without destroying the nonlinear crystal.

The frequencies or wavelengths that are produced in OPG or OPA depend on the phasematching condition, group velocity walk-off and the type of crystal used. Figure 13(b) shows materials that are commonly used for parametric generation in the IR region. BBO has a limited tuning range in the IR range (approximately 1.2–2.8 μm when pumped at 800 nm) but is very efficient owing to the small group-velocity walk-off and high damage threshold. KTP and its analogs rubidium titanyl phosphate and cesium titanyl phosphate (RTA and CTA) are not as efficient as BBO but allow the generation of femtosecond pulses at wavelengths as long as 3–4 μm. There is a variety of crystals suitable for generation of pulses in the mid-IR region such as $AgGaS_2$ and GaSe. However, when these crystals are used to convert directly from the visible to the mid-IR, they suffer from enormous group velocity walk-off, (two-photon) absorption of the pump and very poor efficiency. Therefore, generating mid-IR pulses is typically performed in a two-stage

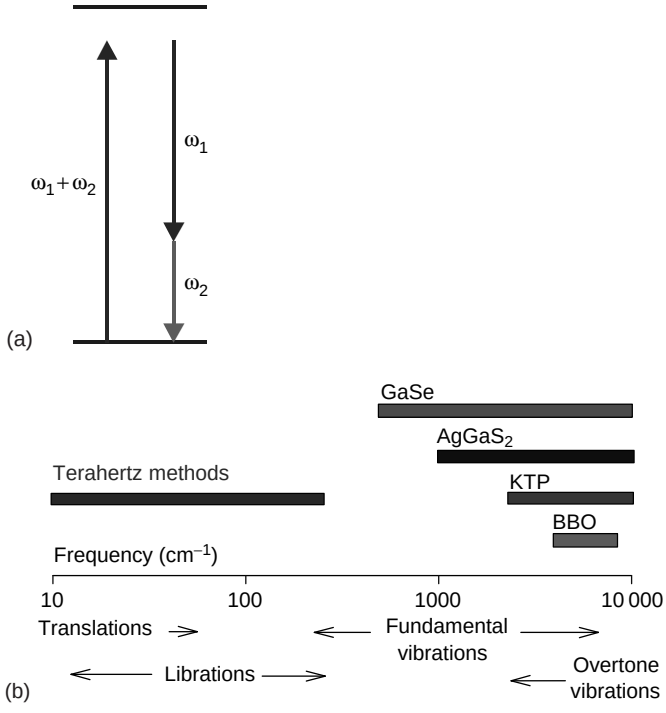

Figure 13 (a) Difference-frequency mixing. A strong femtosecond pulse at frequency $w_1 + w_2$ can mix in a nonlinear crystal with a (weaker) pulse at frequency w_1, to produce a new beam of femtosecond pulses at frequency w_2. (b) Diagram showing the various femtosecond IR tuning ranges that can be obtained using an optical parametric amplification (OPA). Using the common crystals BBO and potassium titanyl phosphate (KTP), tuning between 1 and 3 μm can be obtained. With the more unusual crystals $AgGaS_2$, $AgGaSe_2$ and GaSe, one can obtain radiation to wavelengths as long as 20 μm.

process:[57] an OPA generates two NIR frequencies (e.g. 800 nm → 1.5 μm + 1.7 μm, for example, in BBO) followed by a difference frequency mixing stage (e.g. 1.5–1.7 μm → 12 μm, for example, in $AgGaS_2$).

All known materials suitable as a nonlinear difference-frequency mixing crystal absorb strongly in the far-IR region. GaSe and $AgGaSe_2$ have the longest wavelength cutoff of about 18 μm. In order to produce longer wavelengths, different techniques have to be used (see section 3.5). It has recently been shown that periodically poled crystals such as periodically poled KTP[58] can be used with great success to generate femtosecond IR pulses efficiently.

When femtosecond IR pulses are generated, they inevitably have a very large bandwidth, e.g. about 100 cm^{-1} for a 100-fs pulse, which is clearly much larger than the line width of a typical vibrational transition. This does *not* mean that femtosecond IR pulses are useless for vibrational spectroscopy – quite the contrary! The IR pulse can be spectrally resolved after the sample. The recent availability of IR diode arrays and IR charge-coupled device (CCD) cameras means that an entire IR spectrum can be taken in a single laser shot.[57,59] However, in time-resolved experiments, the broadband IR pulse can excite multiple transitions at once and one has to take account of this carefully in the theoretical analysis of experiments.[60]

3.4 Noncollinear Optical Parametric Amplification

Noncollinear optical parametric amplification (NOPA) is a technique used to generate sub-20-fs tunable visible and NIR pulses.[61] In a collinear geometry, the temporal output of parametric generators and amplifiers is restricted by group-velocity mismatch between the pump and the generated signal and idler fields. In a noncollinear arrangement, this effect can be overcome since only the projection of the idler group velocity on to the seed is important. By arranging the pump and seed incidence angles with respect to the phase-matching angle correctly, this group-velocity mismatch can be zeroed in some nonlinear crystals. A seed pulse, which is a single filament of white-light continuum generated in a 1-mm thick piece of sapphire, is amplified by the frequency-doubled output of a Ti : sapphire amplifier, in type I BBO cut at 31°. The sapphire must be cut such that the optical axis runs perpendicular to the cut face. Type I LBO is used to generate the second harmonic of the Ti : sapphire around 400 nm. The pump beam focused on to the BBO generates a cone of parametric superfluorescence (inset of Figure 14). When the angle of incidence at the crystal is correct, there is no appreciable spatial divergence of the superfluorescence. By directing the continuum seed beam along the cone axis, a large spectral bandwidth from

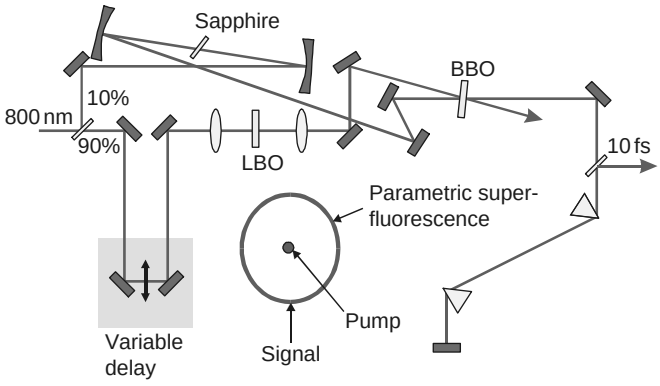

Figure 14 Schematic diagram of a noncollinear OPA. The inset shows the arrangement of the seed beam (the signal) relative to the pump and the generated superfluorescence.

the white light can be simultaneously phase matched. Adjustment of the relative delay between pump and seed and some control of the chirp on the continuum together change the center wavelength and bandwidth of the amplified light. One great advantage of this scheme is that relatively thick crystals can be employed (typically 2 mm), which results in high single-pass gain. The amplified output is then recompressed using a prism pair (BK7 separated by ~60 cm) yielding sub-20-fs visible pulses continuously tunable from 480 to ~700 nm. Pulses as short as 5 fs have been generated[62] using a prism–double chirped mirror recompression scheme, although the mirrors are unavailable commercially at the time of writing. Pumping with only 10 μJ of blue light, 2 μJ can be generated at the signal wavelength. If higher energy is available, a second amplification stage can be added and 10 μJ can be obtained for a 75-μJ pump. Using the same technique, extremely short NIR light can be generated in type II phase-matched BBO pumped at the Ti : sapphire fundamental.

3.5 Terahertz-pulse Generation and Detection

As described above, NIR and mid-IR pulses can be generated using parametric down conversion. However, down conversion cannot produce pulses with a wavelength longer than about 18 μm. Long-wavelength pulses can be generated (and detected) using so-called terahertz techniques. There are effectively two methods for generating subpicosecond terahertz (10^{12} Hz) pulses: photoconduction or optical rectification. In photoconduction, a laser pulse incident on an absorbing semiconductor creates (real) charge carriers in the conduction band. Acceleration of these carriers in an electrical bias field gives rise to a transient photocurrent that radiates electromagnetic waves. In the far field the radiated electric field is given by $\mathbf{E}_R(t) \propto d\mathbf{J}_S(t)/dt$, where $\mathbf{J}_S(t)$ is the time-dependent surface current. This method is typically used

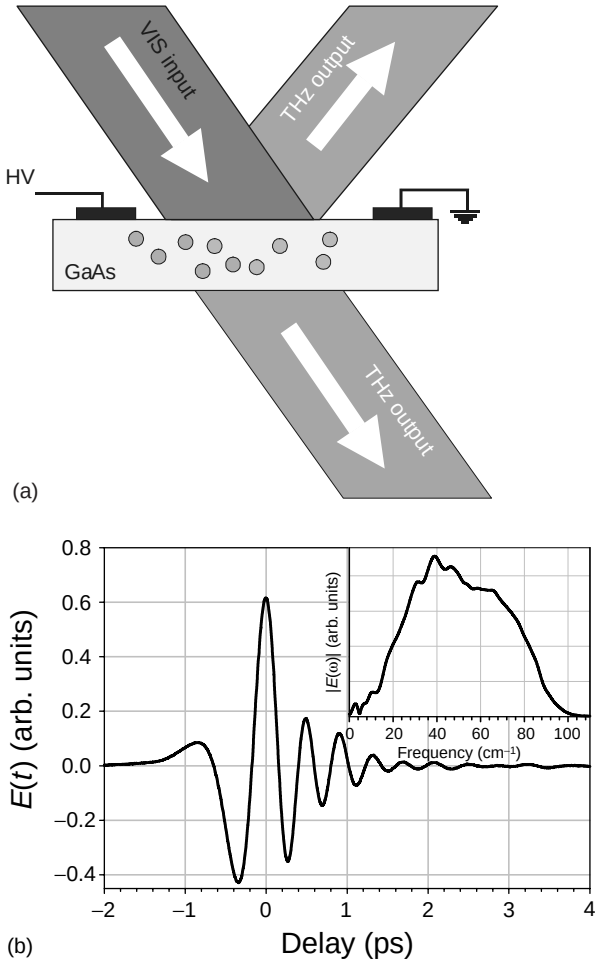

Figure 15 (a) Schematic diagram illustrating the generation of terahertz pulses. A visible femtosecond input pulse irradiates a semiconductor antenna and creates conduction electrons. The acceleration of these electrons in an external DC field results in the emission of two beams of terahertz pulses. (b) A terahertz pulse generated and detected in a 1-mm long ZnTe crystal cut perpendicular to the ⟨110⟩ akis by a 150-fs pulse at 800 nm. The inset shows the amplitude spectrum. The oscillations in the pulse are due to the finite crystal thickness. (1 THz ≈30 cm^{-1}).

in conjunction with an antenna structure (see Figure 15a and b), which allows an external bias field to be applied. An antenna structure ideally suited to be used with low-power mode-locked lasers was developed in the 1980s at Bell Laboratories[63] and IBM,[64] and is now the most common method for generating and detecting terahertz pulses. In such a set-up, two metal electrodes are laid down on a silicon or GaAs substrate, typically with a separation of ∼100 μm. A beam of femtosecond laser pulses is focused between the electrodes, in a spot with a diameter of a few micrometers. On the generation side, the metal electrodes are biased with a few tens of volts and the excitation by the pump laser triggers the emission of terahertz radiation. On the detection side, the incident terahertz beam accelerates carriers created by another visible beam, resulting in a measurable photocurrent. Since the visible beam has to be focused to a very tight spot in this method, only unamplified ultrafast lasers can be used. There is no overriding reason, however, why one should use such closely spaced electrodes. Large-aperture photoconducting antennas work very well for the generation of terahertz pulses when pumped by amplified pulses. The conversion efficiency is about 0.1%. With low repetition rate (10–1000 Hz) ultrafast laser systems, far-IR pulses with energies as high as 1 μJ have been generated.[65]

An external bias field is not strictly necessary for photoconductive generation of terahertz pulses, as real carriers generated by a visible laser pulse can be accelerated in the field of the depletion layer of the semiconductor. This surface field will accelerate the carriers perpendicular to the surface of the semiconductor and hence the terahertz oscillating dipole will be perpendicular to the surface. Therefore, terahertz radiation generated through this effect is only observed if the angle of incidence of the exciting visible laser beam is nonzero. Typically, the effect maximizes at the Brewster angle.

Optical rectification is distinct from photoconduction, in that the visible exciting beam creates virtual rather than real carriers. A more appropriate way to describe this is that the second-order susceptibility, $\chi^{(2)}$, of the crystal is used for difference-frequency mixing. Thus, the second-order polarization can be written in the time domain as Equation (21):

$$P^{(2)}_{\mathrm{THz}}(t) = \varepsilon_0 \chi^{(2)} E_{\mathrm{VIS}}(t) E^{*}_{\mathrm{VIS}}(t) \tag{21}$$

which shows that the electric field of the terahertz pulse has the same shape as the intensity envelope of the visible exciting pulse. In the last few years, it has been discovered that optical rectification is an efficient method for generating terahertz pulses if used appropriately. Since a subpicosecond terahertz pulse has a spatial length comparable to its center wavelength, it travels through a material at its phase velocity. Therefore, for optimum conversion from visible to far-IR wavelengths, one has to match the group velocity of the visible pulse with the phase velocity of the terahertz pulse.[66,67] This condition is met in some zinc blende, large band-gap semiconductors such as ZnTe and GaP when the exciting laser has a center wavelength of ca. 800 nm.

The inverse of optical rectification is electrooptic sampling: a terahertz pulse incident on an electrooptic crystal such as ZnTe will induce a birefringence through the Pockels effect. An ultrafast visible probe pulse with a variable delay copropagating through the same crystal will experience a retardation that can be retrieved with balanced detection. Scanning the relative time delay of

the probe pulse, one can record a time-domain trace of the electric field of the terahertz pulse. Using this method, signal-to-noise ratios, defined as the ratio of the terahertz pulse peak to the noise background, as high as 10^7 have been reported.[68] However, the signal-to-noise ratio with which one can measure the peak of the terahertz pulse is typically of the order of 10^2–10^3 in 100 ms. An exciting new variation on this technique is the use of a chirped probe pulse.[69] A femtosecond pulse at 800 nm can be stretched and chirped to tens of picoseconds using a grating pair. If this chirped pulse is used in the electrooptic sampling process, there will be a relationship between wavelength and relative time delay. Thus, detection of this probe pulse with a spectrometer and diode-array detector allows one to measure the entire terahertz pulse shape in a single laser shot.

As rectification and electrooptic sampling are nonresonant effects, the minimum duration of the terahertz pulses that can be generated or detected is limited only by the thickness of the crystal scaled with the difference in phase and group velocity. Thus, with ca. 10–15-fs exciting pulses at 800 nm, it was shown that terahertz pulses could be generated with detectable frequencies as high as 70 THz.[70] At these large bandwidths, it is unavoidable that the t-ray spectrum will overlap with a photon absorption band in the generating and detecting crystals, leading to large oscillations in the terahertz field trailing the main peak.

The current record highest detectable frequency for a terahertz pulse is ~70 THz, but there is no reason to believe that this could not be improved upon. Using the simple time–bandwidth relation, $\Delta\nu\Delta\tau = 0.32$, it follows that with the shortest visible pulses achievable, ca. 4–5 fs, usable power at frequencies from 0 to 160 THz ($\lambda = 1.8\,\mu m$) could be achieved. As femtosecond lasers continue to shrink in size, it may be expected that ultrafast terahertz devices may well take over from Fourier transform infrared (FTIR) spectrometers as general-purpose IR spectrometers. As an entire terahertz time-domain trace can be acquired in a single shot,[69] these devices would combine the reliability and accuracy of FTIR spectrometry with real-time speeds. The most significant aspect of ultrafast terahertz pulses, however, is that they are synchronized with visible or UV pulses, allowing time-domain spectroscopy.

3.6 Femtosecond Electron Pulses

Very short (picosecond to femtosecond) electron pulses are useful for a variety of applications. For example, picosecond electron pulses have been used as a probe pulse for determining the time-dependent structure of molecules undergoing chemical reactions (see section 5.3). However, such pulses might also be used as a seed for electron accelerators or for the generation of femtosecond X-ray pulses. Current technology for generating femtosecond electron pulses is based on experiments done in the past with picosecond and nanosecond laser pulses.[71–73] A UV laser beam is used to irradiate a metal target. If the photon energy is higher than the work function of the metal (typically 4–5 eV for common transition metals such as gold, silver or tungsten), electrons are ejected into the vacuum through the photoelectric effect. These emitted electrons are electrostatically extracted and accelerated into a narrow beam. In recent experiments (see section 5.3), this technique has been brought into the subpicosecond domain. The main problem in maintaining the time resolution is the space-charge effect: nonrelativistic electrons repel each other through Coulomb repulsion. It is therefore of the greatest importance to accelerate the electrons as quickly as possible and to keep the number of electrons per pulse as low as possible. Thus, it was seen in an experiment[74] that for a 100-μm laser spot size on the photocathode, the electron pulse would broaden to about 15 ps when there were 1000 electrons in the pulse. When the number of electrons per pulse was reduced to 100, the pulse width was less than 1 ps. There is no fundamental reason why one could not work with ten or even one electron per pulse and therefore it should be possible to achieve electron-pulse durations in the order of tens of femtoseconds. Of course, to achieve a reasonable signal-to-noise ratio in an experiment, the pulse repetition rate should be high. Such pulses will be of great value in time-dependent molecular structure determination.

4 TIME-RESOLVED EXPERIMENTS

Most electronic devices cannot measure transients much faster than about 1 ns. Although there are specialized electronic devices such as streak cameras that may be able to resolve picosecond or even hundreds of femtosecond transients in real time, in most cases it makes more sense to look for alternative detection techniques. The techniques that are used most frequently are based on auto- or cross-correlation of two beams of femtosecond pulses (see Figure 16a). If the sample is a nonlinear crystal used for sum-frequency generation, this technique can be used to determine the shape and relative arrival time of two short pulses. If the sample contains molecules or atoms that resonantly absorb the incident radiation, the experiment is a pump–probe experiment.

4.1 Auto- and Cross-correlation

In an autocorrelator, an incoming beam of pulses is split in two. One beam travels through an optical path with

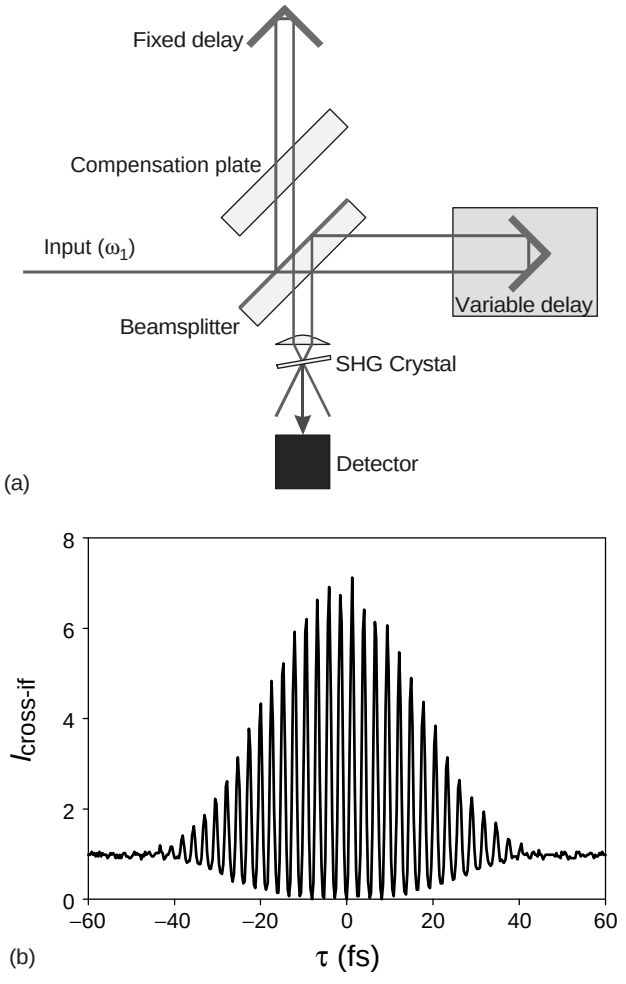

Figure 16 (a) Schematic diagram illustrating the layout of an autocorrelator. Two laser beams of femtosecond pulses at frequency w_1 are overlapped in a nonlinear crystal such as BBO. The sum-frequency signal at frequency $2w_1$ as a function of relative time delay is proportional to the shape of the pulse. (b) Interferometric autocorrelation of a 25-fs fwhm laser pulse at 800 nm.

a fixed length, the other through a path that includes an optical delay line. An optical delay line consists simply of a pair of mirrors or a retro-reflector mounted on a motorized translation stage or a sine-wave-driven loudspeaker. In such a set-up, the spatial position of the mirrors on the translation stage is related directly to the relative time delay between the two beams of pulses. For example, if the optical delay line is translated by $L = 1\,\mu\text{m}$, this corresponds to a change in relative time delay of $\tau = 2L/c \approx 6.6\,\text{fs}$. Both beams are focused in a nonlinear crystal such as BBO or KDP in order to produce second-harmonic radiation. Phase matching[56] in the crystal is used to produce a beam at the second-harmonic frequency in which one photon has been taken from one beam and one from the other. Alternatively, two-photon absorption in a photodiode may be used to provide the required second-order response.[75] The averaged measured auto- or cross-correlation signal then has the form (Equation 22)

$$I_{\text{cross}}(\tau) \propto \left|\chi^{(2)}\right|^2 \int I_{w_1}(t) I_{w_2}(t-\tau)\,\mathrm{d}t \qquad (22)$$

where $\chi^{(2)}$ is the second-order susceptibility of the nonlinear crystal and τ is the relative delay time $t_1 - t_2$ between the two pulses. Of course, the cross-correlation signal consists itself of a train of femtosecond pulses but since one is only interested in the *average* signal as a function of the relative time delay, no fast detector is required. Since the nonlinear crystal is chosen such that it does not exhibit any time-dependent processes of its own, the cross-correlation signal as a function of time delay is proportional to the shape of the incoming pulses. For example, in the case of an autocorrelation of a pulse with a Gaussian envelope, the autocorrelation signal as a function of delay has itself a Gaussian shape. In this example, one can measure the fwhm of the autocorrelation signal and find the width of the intensity envelope of the pulse by multiplying by 0.71. The value of the conversion factor depends on the pulse shape and a list of conversion factors can be found in Table 4. In practice, it may be wise to use nonlinear curve fitting to determine the pulse shape and corresponding conversion factor.

Clearly, the auto- or cross-correlation signal contains limited information about the pulse shape. For example, an asymmetric pulse shape will go undetected in an autocorrelation. More serious is that an autocorrelation will provide almost no information about possible chirp on the pulse (see section 2.2). If the pulse is chirped, the autocorrelation will be broader than might be expected from the pulse spectrum. Table 4 has a column with time–bandwidth products, that is, the product of the fwhm of the intensity envelope of the pulse in the time domain and the frequency domain. However, checking that the time–bandwidth product is close to that expected for a given pulse shape is *not* a very good method of making sure that the pulse is chirp free.

A better method for detecting chirp is the measurement of an interferometric autocorrelation and is taken by overlapping the two input beams. The correlation signal is now much more complicated[77] and oscillates at frequencies corresponding to the laser fundamental and second harmonic. Since the second-harmonic intensity is proportional to the square of the incident intensity, the detected second-harmonic intensity as a function of delay is (Equation 23)

$$I_{2w}(\tau) = \frac{1}{T}\int_{-T/2}^{T/2} \left|[E(t) + E(t-\tau)]^2\right|^2 \mathrm{d}t \qquad (23)$$

Table 4 Second-order autocorrelation functions and time–bandwidth products for various pulse-shape models,[76] where τ_p = pulse width (fwhm), τ_G = autocorrelation width (fwhm) and $\Delta\nu$ = spectral width (fwhm)

$I(t)$ $(x \equiv t/T)$	$\Delta\nu\Delta\tau_p$	τ_p/T	$G_0^2(\tau)$ $(y \equiv \tau/T)$	τ_G/T	τ_p/τ_G
Gaussian $I(t) = e^{-x^2}$	0.4413	$2\sqrt{\ln 2}$	$e^{-y^2/2}$	$2\sqrt{2\ln 2}$	0.7071
Diffraction function $I(t) = \dfrac{\sin^2 x}{x^2}$	0.8859	2.7831	$\dfrac{3}{2y^2}\left(1 - \dfrac{\sin 2y}{2y}\right)$	3.7055	0.7511
Hyperbolic sech $I(t) = \operatorname{sech}^2 x$	0.3148	1.7627	$\dfrac{3(y\coth y - 1)}{\sinh^2 y}$	2.7196	0.6482
Lorentzian $I(t) = \dfrac{1}{1+x^2}$	0.2206	2	$\dfrac{1}{1+(y/2)^2}$	4	0.5000
One-sided exponential $I(t) = \begin{cases} e^{-x} & \wedge t \geq 0 \\ 0 & \wedge t < 0 \end{cases}$	0.1103	$\ln 2$	$e^{-\lvert y\rvert}$	$2\ln 2$	0.5000
Symmetric two-sided exponential $I(t) = e^{-2\lvert x\rvert}$	0.1420	$\ln 2$	$(1 + 2\lvert y\rvert)e^{-2\lvert y\rvert}$	1.6783	0.4130

where T is the measurement time, and $T \gg \tau$. Figure 16(b) shows an experimental interferometric autocorrelation trace of a 25-fs 800-nm pulse. If the pulse is bandwidth limited, the interferometric autocorrelation signal yields a ratio between peak and background of 8 : 1. Linear chirp (caused by GDD) is clearly visible as the peak-to-background ratio is much less than 8 : 1 in that case. Nonlinear chirp (caused, for example, by residual TOD) is clearly visible as a ''pedestal'' on the interferometric autocorrelation.

Another useful technique for characterizing femtosecond pulses is called frequency-resolved optical gating (FROG)[78] with which both the intensity and phase of a femtosecond pulse can be determined. The critical feature of FROG is that it measures the (second- or third-order) autocorrelation as a function of both time delay and frequency (see Figure 17). As before, a beam of femtosecond pulses is split in two and recombined on a nonlinear crystal. In this case, the two beams are focused on to the nonlinear crystal using a cylindrical lens. As a result, different positions on the crystal correspond to different relative delay times. If the crystal produces the second harmonic of the incident beams, the emergent beam will have the autocorrelation trace spatially encoded on to it. If the signal beam is sent through a spectrometer, a two-dimensional detector such as a CCD camera can be used to measure a signal that depends on delay in one direction and frequency in the other. Various nonlinearities can be used with the FROG technique, such as SHG and self-diffraction (effectively the OKE in a piece of glass; see section 3.1).

In the polarization-gate arrangement of self-diffraction,[79] the probe pulse $E(t)$ passes through crossed polarizers and is gated at the nonlinear medium by the gate pulse $E(t-\tau)$, which has a 45° relative polarization. A cylindrical lens focuses each beam to a line in the sample (e.g. a piece of glass) so that the delay varies spatially across the sample. Consequently, at the spectrometer,

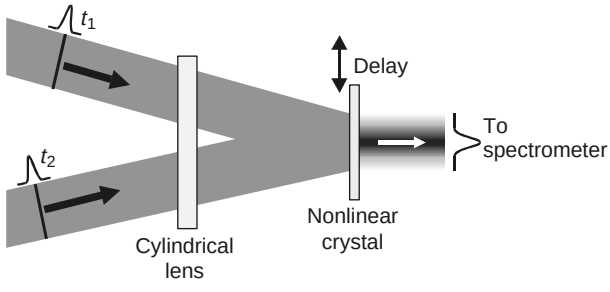

Figure 17 Experimental arrangement for single-shot FROG. Two beams of femtosecond pulses are focused with a cylindrical lens on to a nonlinear crystal, e.g. one that generates the second-harmonic of the input beam. Because of the focusing geometry, the position on the nonlinear crystal corresponds directly with time delay. This allows one to measure the correlation trace as a function of both time and frequency.

the delay τ varies along the slit, whereas the frequency w varies in a direction perpendicular to this. For such an arrangement, the resulting signal-pulse electric field is given by Equation (24):

$$E_{sig}(t, \tau) \propto \chi^{(3)} E(t)|E(t-\tau)|^2 \tag{24}$$

where $\chi^{(3)}$ is the third-order susceptibility of the sample (i.e. the strength of the OKE). The FROG trace can be considered a ''spectrogram'' of the field $E(t)$ as the signal intensity is given by Equation (25):

$$I_{FROG}(w, \tau) \approx \left| \int_{-\infty}^{\infty} E(t) g(t-\tau) e^{-iwt}\, dt \right|^2 \tag{25}$$

where the variable-delay gate function $g(t-\tau)$ is equal to $|E(t-\tau)|^2$. This quantity can be thought of as a gate that chooses a slice of the time-varying signal pulse.

At each delay, the signal consists of different frequency components, so the gate function builds up a spectrum of the pulse for every value of τ. For a transform-limited pulse, it is expected that only frequencies within the

bandwidth of that pulse would be resolved and that the instantaneous frequency remains the same at each point in time. However, for a chirped pulse, where lower frequencies lead higher ones or vice versa, the frequency-resolved trace will be considerably different, since the instantaneous frequency is a function of time. Since the phase of the signal pulse is contributed only by $E(t)$ [$E(t-\tau)$ appears as the square, so all phase information is lost], the phase can be retrieved from a FROG trace. This is achieved using an iterative Fourier-transform algorithm.

Ultrashort pulse characterization techniques generally require instantaneously responding media. The polarization gate geometry FROG technique uses the electronic Kerr effect, which is accompanied, however, by a Raman-ringing effect. The slower nuclear motion of the material must therefore be considered in the iterative algorithm used to retrieve the pulse phase and intensity. The pulse-retrieval algorithm can be modified[80] by including terms due to the slow response of the medium in the signal-field equation. Such problems with a slow response of the correlating medium can be avoided by using two-photon absorption in a diode.[75]

4.2 Pump–Probe Techniques

Most ultrafast spectroscopy experiments use the pump–probe technique, which is very similar to the cross-correlation technique described above. In pump–probe spectroscopy the pump beam is typically much stronger than the probe beam, the two beams have a different center wavelength (or the probe may not even be a laser beam), and the sample tends to be more interesting. As in the cross-correlation technique, the femtosecond time resolution is obtained by sending one of the beams through a motor-driven optical delay line. The (relatively) strong pump beam initiates some process of interest, e.g. a chemical reaction. The probe beam, entering the sample later, will be amplified, attenuated or refracted because of the changes taking place in the sample. There are so many variations of this scheme and literally thousands of experimental examples that it would be pointless to list them all. Therefore, two examples of the pump–probe technique will be described in some detail here to convey the general idea.

Figure 18 shows a very typical pump–probe spectroscopy set-up. A relatively strong pump beam is sent through a (motorized) optical delay line and focused into the sample where it initiates some chemical reaction. In many cases, the pump beam will be modified, e.g. by doubling or tripling its frequency through SHG or THG. A (small) fraction of the pump beam is split off by an optical beamsplitter and converted to another wavelength. In this example, a white-light continuum is generated as a probe but one could also use other conversion techniques to make probes at widely varying wavelengths. In any event, the probe pulse is sent through another optical delay line and focused into the sample. One may temporarily replace the sample by a nonlinear crystal to determine at which setting of the optical delay lines the pulses overlap in the sample. In Figure 18, the white-light probe is spectrally resolved by a spectrometer after the sample in order to measure the transient transmission spectrum of the sample. The signal measured as a function of the pump–probe delay time reflects the creation and destruction of chemical species in the sample. However, on short timescales ($\sim$<1 ps), there are numerous phenomena such as cross-phase modulation (see section 3.1) that may complicate the signal.[45,60] A variation on the pump–probe technique is the photon echo.[56] Photon echoes may be used to remove inhomogeneous broadening from an absorption spectrum and can therefore be very useful in analyzing complex samples.

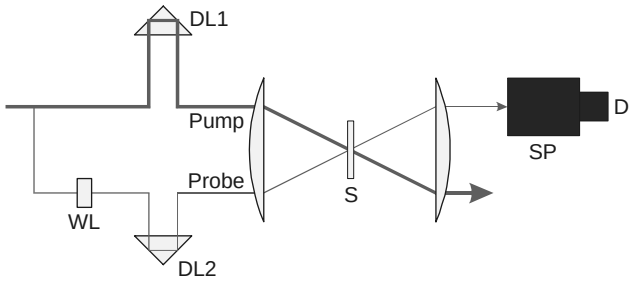

Figure 18 "Classical" pump–probe spectroscopy set-up. A relatively strong pump beam is sent through an optical delay line (DL1) and focused into the sample (S). A small fraction of the pump beam is split off and converted to another wavelength. In this example, a white-light continuum is generated as a probe, which is sent through another optical delay line (DL2) and into the sample. After the sample, the white-light probe is spectrally resolved by a spectrometer (SP) before being detected by a "slow" detector (D).

In the above example of the pump–probe technique, both the pump and probe were laser pulses. However, lasers can also be used to make pump and probe pulses of an entirely different kind. Figure 19 shows an example where femtosecond laser pulses are used to generate and gate voltage pulses.[81–84] A short laser pulse can be used to create carriers in the conduction band of a semiconductor and thereby create a femtosecond voltage pulse that can be sent down a transmission line deposited on to the sample. The voltage pulse can be picked up, for example, by a STM tip. If the current flowing through the STM tip is gated by a second laser pulse, the averaged tunnel current can be measured as a function of pump–probe delay in addition to the spatial position of the tip. Therefore, this type of pump–probe technique provides both very high temporal resolution

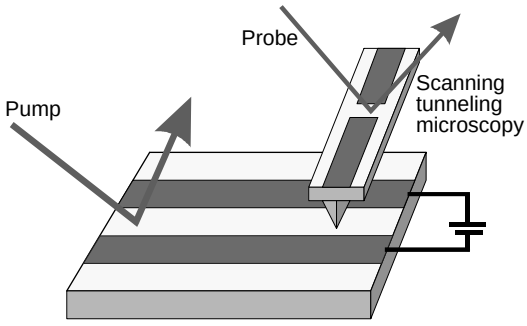

Figure 19 Unconventional pump–probe technique. In this example, the pump beam excites electrons in the conduction band of a semiconductor, thereby creating a femtosecond voltage pulse in the metal transmission line deposited on top of the semiconductor sample. The voltage pulse can be measured by an scanning tunneling microscopy (STM) tip. If the current flowing through the STM cantilever is itself gated by a probe pulse, time- and space-resolved measurements can be performed.

and spatial resolution. There are many other examples of unconventional pump–probe techniques. The probe may consist of X-ray pulses, electron pulses or any other kind of pulsed particle beam. The only critical requirement is that the pulses in the pump beam are synchronized to those in the probe beam.

5 APPLICATIONS

As ultrafast lasers are becoming smaller and easier to use, they will find increasingly down-to-earth applications. For example, IR generation using ultrafast lasers may become so simple and cheap that its advantages can be used: spatially coherent beams (resulting in better focusing and directionality), coherent detection (allowing one to measure refractive indices directly without resorting to the Kramers–Kronig relations), broadband (allowing single-shot detection of an entire spectrum) and more power at ''odd'' wavelengths (especially in the far-IR region). One of the main advantages of ultrafast lasers is, of course, that they allow time-resolved experiments with which one can observe transient species. Another advantage is that short pulses with modest energy can have huge peak power. This makes femtosecond pulses very suitable for laser ablation of materials, multiphoton absorption (for imaging of biological materials), fragmentation (e.g. of DNA into fragments that may be analyzed using MS), etc. The high peak power also permits the efficient conversion to other wavelengths using nonlinear crystals. A slightly unexpected recent observation is that when femtosecond lasers are used for machining the resulting cuts are much cleaner because the laser pulses turn the material into a plasma rather than melting it. The number of applications of ultrafast lasers is already large and will only grow. It would be impossible to describe all these applications in the limited space available here. Therefore, a few key applications will be described.

5.1 The Study of Fast Chemical Reactions

In principle, there is no difference in the information that can be obtained from a frequency-resolved or a time-resolved experiment. In a frequency-resolved spectrum, a vibronic transition may show up as a series of sharp absorption lines. In the equivalent time-resolved experiment, one will observe quantum beats whose periods correspond to the inverse of the spacings between the absorption lines. In practice, however, there may be differences. For example, even in the gas phase, the spacing between the absorption lines may be so small that it is hard to resolve them. More importantly, in the solution phase, the molecule under study will couple to the degrees of freedom of the surrounding bath. Strictly, the Schrödinger equation for the liquid could be solved, which would show that the dynamics in the liquid in fact correspond to about one-trillion-trillion (10^{24}) well-defined quantum states. Most of these bath states will be coupled to the vibronic states in the molecule, resulting in the broadening of the transition. In such a case, a spectrally resolved experiment will provide little information about the dynamics of the molecule or the dynamics of a chemical reaction that one would like to study. Even hole-burning spectroscopy will not provide much more information in most cases. Only time-resolved pump–probe techniques can elucidate the molecular dynamics.

In the 1980s and 1990s, a series of experiments were performed by a variety of groups which came to be known as ''femtochemistry'' or ''femtobiology''. These experiments exploited the property that if a molecule is excited with a laser pulse shorter than the oscillation period of relevant vibrations in the molecule, a coherent vibrational wavepacket is created in the excited state (see Figure 20a and b). Vibrations with a period shorter than the pulse width are simply not coherently excited and do not give rise to quantum beats.

The ''hydrogen atom'' of femtochemistry is the diatomic molecule NaI that was extensively studied in the gas phase.[13] When NaI is excited by a femtosecond UV pulse (see Figure 21a and b), a wavepacket is created on the repulsive excited state, which (at large interatomic distances) corresponds to the ion pair Na^+ and I^-. However, this repulsive potential forms an avoided crossing with the ground-state potential, which (at large interatomic distances) corresponds to the radical pair Na + I. If the system is probed in the excited-state potential well, it is seen that the wavepacket coherently oscillates

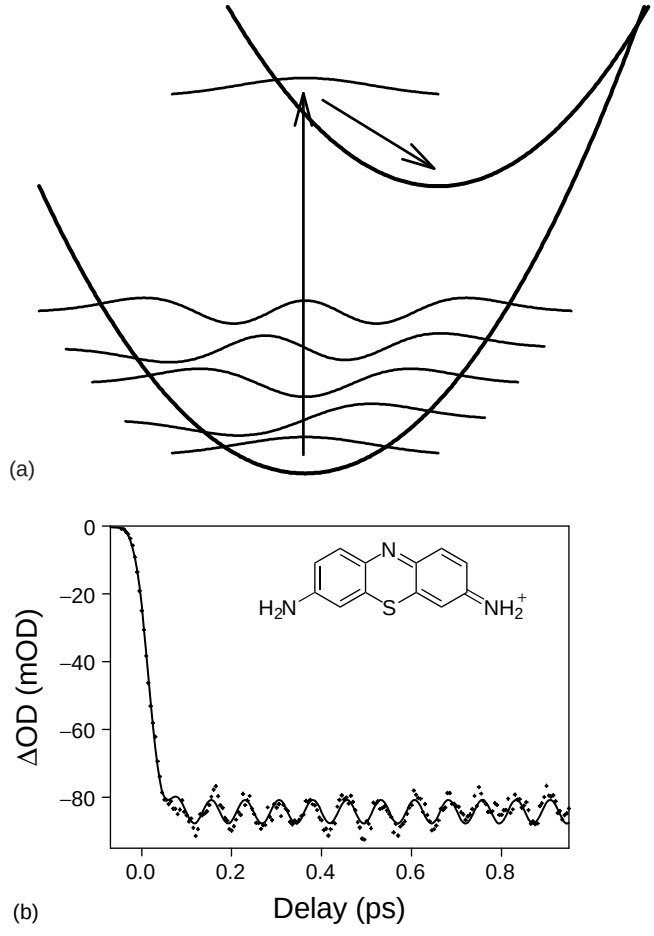

Figure 20 (a) Schematic diagram of a vibronic transition excited by a pulse whose width is smaller than the vibrational period. The pulse creates a coherent vibrational wavepacket in the excited electronic state that will oscillate in the excited-state potential well. (b) Time-resolved 600-nm pump, 700-nm probe signals in the dye molecule thionine studied with 42-fs time resolution. The signal is stimulated emission from the excited electronic state and the oscillations correspond to a vibrational mode at 443 cm^{-1} in the excited-state potential well.

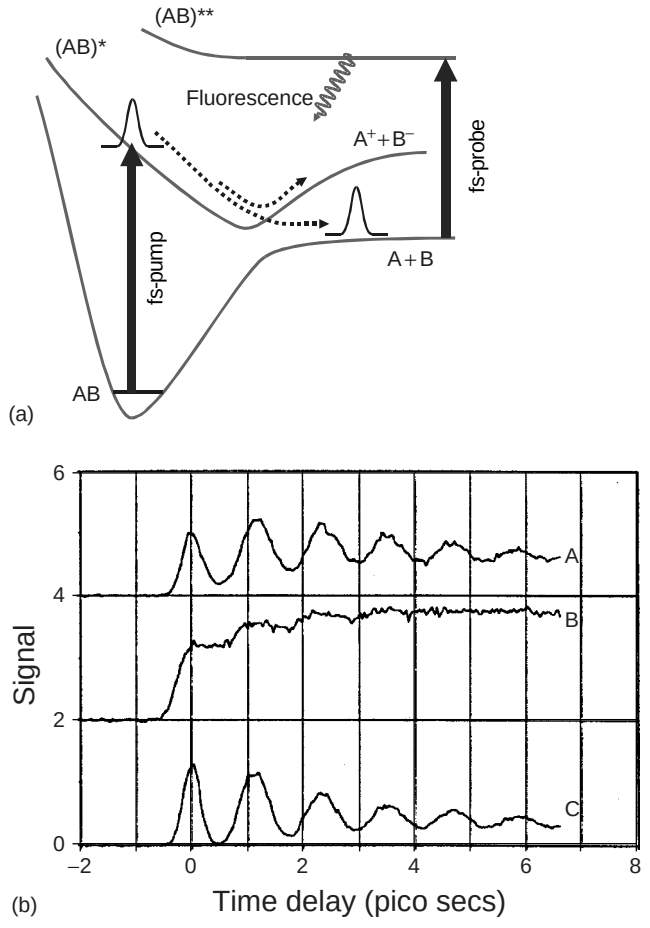

Figure 21 (a) Simple diagram depicting a typical coherent dissociation reaction. The pump pulse excites a small molecule to its first excited state. If the pump pulse is shorter than the vibrational period, it may create a coherent wavepacket that will oscillate in the excited-state potential well. In this diagram, the molecule splits into two fragments consisting of either two radicals or two ions. A probe pulse excites the molecule to a third state, from which it fluoresces back to the ground state. The total fluorescence is measured as a function of pump–probe delay. (b) Pump–probe results[86] from NaI with $\lambda_{pump} = 310$ nm. (A) $\lambda_{probe} = 580$ nm; (b) $\lambda_{probe} = 589$ nm (on resonance); and (C) $\lambda_{probe} = 612$ nm. (Reproduced from Rosker et al.[86] by permission of Elsevier Science. © Elsevier Science BV, 1988.)

in the bound state. However, if the sodium radical is probed by inducing fluorescence with the probe pulse, it is seen that the population of the radical increases in a stepwise fashion. Therefore, such an experiment shows that the chemical reaction (a dissociation in this case) is a quantum-mechanical process in which a fraction of the bound wavepacket tunnels to the state of dissociated radicals each time the wavepacket travels through the crossing region. Interestingly, it is possible to use quantum mechanical interference of wavepackets to steer a reaction in a desired direction and away from undesired directions. This is referred to as coherent control and has been applied on small molecules with varied success.[85]

A study, such as that on NaI described above, becomes interesting if one can compare the behavior in the gas phase with that in the condensed phase.[87] Various molecules that had been studied in the gas phase have now been studied in solution where again one could observe quantum beats due to vibrational wavepackets. Examples are HgI_2[88] and I_2.[89,90] Vibrational quantum beats have now been observed in a large variety of molecules in the condensed phase, including proteins.[91] In these large, complicated systems, quantum beats provide a unique opportunity to determine the potentials relevant for chemical and biological reactions. Not least, the femtochemistry technique may be used to detect

short-lived intermediates that would be invisible when ordinary spectrally resolved techniques were used. A recent experiment[1] has shown that femtochemistry can be combined with MS: pump and probe laser beams were crossed with a molecular beam and radical fragments were detected with MS as a function of pump–probe delay. The technique was used to study Diels–Alder reactions and the concept of concertedness and may well find more general use in analytical chemistry. Now that high-repetition rate, high-power lasers are available, ultrafast lasers may be used to make a variety of elusive molecules that normally occur only in the atmosphere or in space.

5.2 Imaging

Nonlinear ultrafast optics can be of immense value for (biological) imaging studies. Femtosecond lasers can be used to perform multiphoton absorption confocal-imaging studies. Using this technique, one can image the spatial distribution of one specific molecule inside a living cell.[92] Tunable femtosecond NIR pulses are ideal for this purpose as scattering and damage to the cell are reduced compared with UV radiation. A new alternative involving THG at the focus of a microscope has been used recently in imaging applications.[93] At an interface, giving rise to a slight change in refractive index or third-order nonlinear susceptibility, THG becomes phase matched.[94] The UV light generated can be detected using a photomultiplier tube or CCD camera. The conversion efficiency is low (10^{-8}), but at the tight focus of a high numerical-aperture objective lens, a fluence of 100–300 GW cm^{-2} (a few nanojoules per pulse) is enough to generate a detectable third-harmonic signal without damage to the sample. The technique benefits from being background free. NIR light at 1.2 μm has been employed,[95] giving a third-harmonic signal at 400 nm away from potentially harmful UV wavelengths, which would damage delicate (possibly living) specimens. The chirp induced by the lens is also much smaller in the NIR region. In distinct contrast to multiphoton absorption of samples tagged with fluorescent probes, no reduction in signal is observed over time since the sample is not repeatedly bleached. Scanning mirrors are used to provide traveling Lissajou patterns giving a nearly uniform sample illumination and the image is recorded on a CCD camera. An example image[95] is shown in Figure 22(a). Here, a rhizoid (a tubular single cell) tip from chara plants (green algae) is shown. The bright spots are stratoliths, vesicles containing $BaSO_4$ crystals, which flow within the cell and are necessary for the gravitational response of the alga. The CCD camera detects the motion of these stratoliths over time. This example shows that the technique is applicable to the same systems as more conventional

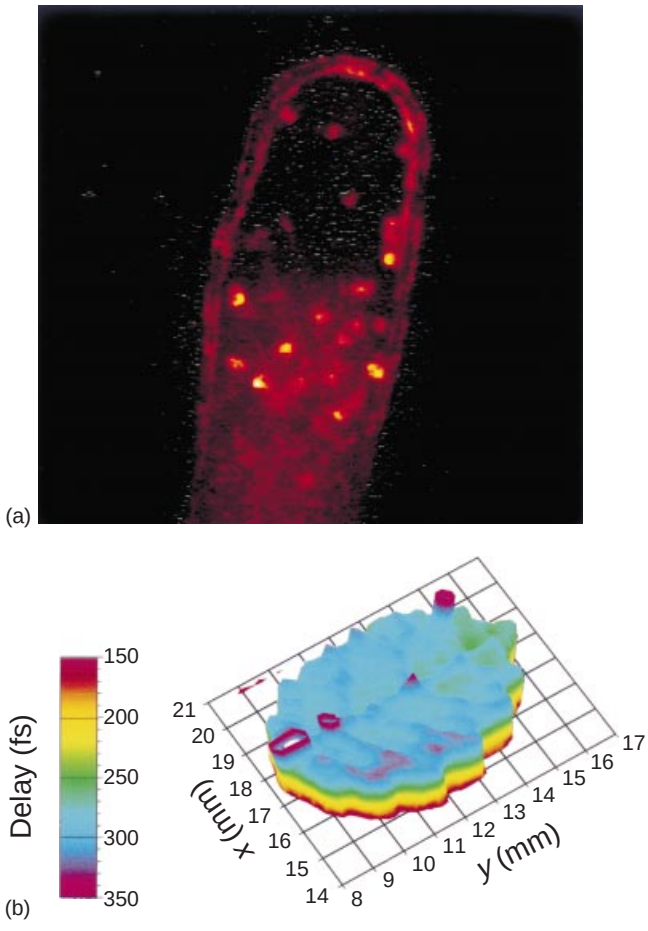

Figure 22 (a) THG image[95] at root tip showing motion of stratoliths. The image is approximately 75 × 75 μm^2. (Reproduced from J.A. Squier, M. Muller, G.J. Brakenhoff, K.R. Wilson, *Opt. Express*, **3**(9), 315–324 (1998), by permission of the Optical Society of America, 1998.) (b) THz image of a bonsai leaf taken by plotting the transmission time as a function of position.[99]

phase-contrast microscopy and will surely be developed further as techniques for optimizing the duration of the pulse at the objective are developed.[96–98]

The frequency range between ca. 100 GHz and a few terahertz has not been studied very well, as not many light sources are available. FTIR spectrometers typically peter out at frequencies below about 50 cm^{-1} (1.5 THz), even when equipped with bolometric detectors and far-IR optics. Microwave devices may go to frequencies as high as 1 THz but usually have poor tunability. However, this frequency range is of great interest as many low-frequency vibrational and rotational modes absorb here. The pseudo-band gaps of superconductors and inter-band gaps of semiconductor heterostructures are also in this range. An exiting new application of terahertz pulses is t-ray imaging. T-ray imaging was first performed at Bell Laboratories:[100,101] a beam of terahertz pulses was focused to a tight spot and a sample was scanned through

the beam. Owing to the long wavelengths at ca. 1 THz, spatial resolution was limited to about 1 mm. However, because the transit time of subpicosecond terahertz pulses can be measured with an accuracy of a few femtoseconds (see Figure 22b), it is possible to make tomographic images.[100] Thus, by measuring the internal reflections in a sample, for example, the various surfaces in a floppy disk, it is possible to detect hidden features with a depth resolution much higher than the wavelength. Very recently, several attempts have been made to improve the lateral resolution by applying near-field techniques such as using small apertures in front of the sample[102] or terahertz pulse generation in subwavelength regions.[99] It was shown recently[103] that electrooptic sampling can be performed in parallel using a large-area electrooptic crystal and an unfocused probe beam, thus allowing the acquisition of t-ray images in real time.

Using a technique analogous to ultrasound, optical-coherence tomography utilizing femtosecond lasers has permitted micrometer resolution in real-time imaging applications, particularly in biomedicine.[104] Cross-sectional images are made in a similar manner to the terahertz-imaging application by measuring the ''echo'' time of backscattered light using interferometric methods. Since the axial resolution is limited by the coherence length of the light, short-pulse Ti : sapphire and particularly NIR Cr : forsterite lasers are seen as attractive sources. An image is measured by building up the backscattered pattern at several transverse positions and these high average-power lasers are ideal for imaging at a few frames per second.

5.3 Structure Determination: Electron Beams and X-rays

Time-resolved pump–probe spectroscopy has been used for a long time to study chemical reactions. Often such spectroscopy relies on excitation and probing at visible wavelengths and transient visible spectra have to be carefully analyzed and interpreted to find out what the reaction products are. More recently, several groups have started to use femtosecond IR pulses in the hope that transient IR spectra will give more direct information about which chemical bonds are broken or formed. However, neither visible nor IR spectroscopy provides direct information about the spatial atomic structure of a given reaction intermediate.

X-ray diffraction has been used for close on a century to determine the atomic structure of crystals. Especially in the life sciences this has resulted in a much better understanding of the structure of proteins and other biomolecules and hence to a better understanding of the fundamentals of biochemistry. Because of the great absorption of electrons by materials, time-resolved electron-diffraction experiments have so far only been performed in the gas phase and on surfaces. However, as steady-state electron diffraction has also been used to determine the structure of proteins in the solid state,[105] femtosecond time-resolved electron diffraction in the solid state may also become a possibility. Electrons at present provide the most structural information for a given amount of radiation damage.[106] The atomic cross-section of carbon for (elastic or inelastic) scattering of electrons is more than six orders of magnitude larger than that of X-rays. Furthermore, radiation damage by 80–500-keV ($\lambda = 0.043$–0.017 Å) electrons is 400–1000 times less than that of $\lambda = 1.5$ Å X-rays.[106] Clearly, it would be a great advantage if one could apply the technique of diffraction on a femtosecond timescale. Modern synchrotron facilities such as the European Synchrotron Radiation Facility (ESRF) in Grenoble, France, and the Advanced Light Source (ALS) in Berkeley, CA, USA, now make it possible to study structural dynamics using time-resolved X-ray crystallography on a nanosecond timescale.[107,108] However, many chemical and biological reactions take place on a picosecond or even femtosecond timescale. Many research groups around the world are now working towards the goal of femtosecond timescale diffraction. The technology of generating femtosecond X-ray or electron pulses is described in sections 3.2 and 3.6.

A series of (sub)picosecond time-resolved electron-diffraction experiments was recently performed on gas phase samples in a molecular beam (Figure 23a and b).[109,110] In these experiments, electron pulses were generated by exciting a back-illuminated photocathode with 400-fs 307-nm laser pulses at a 30-Hz repetition rate. The electron pulses (~6000 electrons) were then accelerated to 18.8 keV and focused with the 307-nm pump beam into a gas jet containing the sample. Two-dimensional electron diffraction patterns were recorded as a function of pump–probe delay using a CCD camera fiber-coupled to an image intensifier. The time resolution (determined by space–charge effects) was about 7 ps. In these experiments, dissociation reactions in, for example, CF_2I_2 and $Fe(CO)_5$ were studied. The method allowed the observation of rare reaction intermediates and, most importantly, the determination of their spatial structure. Picosecond time-resolved electron diffraction experiments have also been performed on surfaces. For example, the effect of melting a Pb (110) surface has been studied.[72]

Generating femtosecond hard X-ray pulses is much more difficult than generating electron pulses, which may explain the small number of unique experiments.[53] All ultrafast X-ray diffraction experiments to date[53,111] have studied the lattice expansion of semiconductors, metals

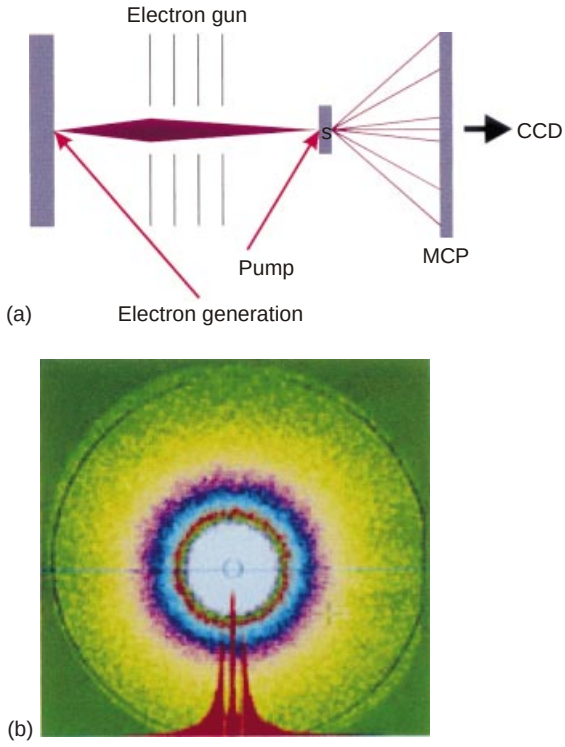

Figure 23 (a) Schematic diagram of a time-resolved electron-diffraction experiment. A strong femtosecond laser pulse irradiates a metal target and produces femtosecond electron pulses. The electrons are accelerated by an electron gun and focused into a sample. Diffracted electrons are detected by an imaging multichannel array plate (MCP) and CCD detector. If the sample is pumped by another beam of femtosecond pulses, one can detect the change in the diffraction pattern induced by the pump. (b) Femtosecond electron-diffraction pattern.[74,109,110] Picture courtesy of the California Institute of Technology.

or organic films under intense laser irradiation. In such an experiment, one typically selects one diffraction peak and measures the amount of diffracted X-rays as a function of the pump–probe delay or the shift or broadening of the diffraction peak. The changes in the diffraction peak reflect, for example, the expansion of the lattice and sound waves bouncing through the crystal.[112] It may be a while before the technique is mature enough to study the time dependence of complete diffraction patterns.

ACKNOWLEDGMENTS

We gratefully acknowledge financial support from the Engineering and Physical Sciences Research Council (EPSRC) and the Royal Society. In addition, we thank Professor Robin M. Hochstrasser for his support and guidance over the years.

ABBREVIATIONS AND ACRONYMS

BBO	β-Barium Borate
CCD	Charge-coupled Device
CPA	Chirped-pulse Amplification
CPM	Colliding-pulse Mode-locked
CTA	Cesium Titanyl Phosphate
CW	Continuous Wave
FHG	Fourth-harmonic Generation
FOD	Fourth-order Dispersion
FR	Faraday Rotator
FROG	Frequency-resolved Optical Gating
FTIR	Fourier Transform Infrared
fwhm	Full Width at Half-maximum
GDD	Group Delay Dispersion
GVD	Group Velocity Dispersion
IR	Infrared
KDP	Potassium Dihydrogenphosphate
KLM	Kerr Lens Mode Locking
KTP	Potassium Titanyl Phosphate
LBO	Lithium Triborate
MCP	Multichannel Array Plate
MS	Mass Spectrometry
NIR	Near-infrared
NOPA	Noncollinear Optical Parametric Amplification
OKE	Optical Kerr Effect
OPA	Optical Parametric Amplification
OPG	Optical Parametric Generation
PC	Pockels Cell
RTA	Rubidium Titanyl Phosphate
SHG	Second-harmonic Generation
STM	Scanning Tunneling Microscopy
TFP	Thin-film Polarizing Beamsplitter
THG	Third-harmonic Generation
TOD	Third-order Dispersion
UV	Ultraviolet

RELATED ARTICLES

Biomedical Spectroscopy **(Volume 1)**
Biomedical Spectroscopy: Introduction • Fluorescence Spectroscopy In Vivo • Infrared Spectroscopy in Microbiology • Optical Coherence Tomography

Biomolecules Analysis **(Volume 1)**
Infrared Spectroscopy of Biological Applications • Single Biomolecule Detection and Characterization

Clinical Chemistry **(Volume 2)**
Infrared Spectroscopy in Clinical Chemistry • Ultraviolet/Visible Light Absorption Spectrophotometry in Clinical Chemistry

Environment: Trace Gas Monitoring **(Volume 3)**
Environmental Trace Species Monitoring: Introduction • Laser Absorption Spectroscopy, Air Monitoring by Tunable Mid-infrared Diode • Laser-induced Breakdown Spectroscopy, Elemental Analysis

Environment: Water and Waste **(Volume 3)**
Infrared Spectroscopy in Environmental Analysis

Peptides and Proteins **(Volume 7)**
X-ray Crystallography of Biological Macromolecules

Atomic Spectroscopy **(Volume 11)**
Laser Ablation in Atomic Spectroscopy • Laser-induced Breakdown Spectroscopy

Electroanalytical Methods **(Volume 11)**
Ultrafast Electrochemical Techniques

Electronic Absorption and Luminescence **(Volume 12)**
Fluorescence Imaging Microscopy • Fluorescence Lifetime Measurements, Applications of

Infrared Spectroscopy **(Volume 12)**
Infrared Spectroscopy: Introduction

Kinetic Determinations **(Volume 12)**
Kinetic Determinations: Introduction

Kinetic Determinations cont'd **(Volume 13)**
Instrumentation for Kinetics

Mass Spectrometry **(Volume 13)**
Time-of-flight Mass Spectrometry

X-ray Spectrometry **(Volume 15)**
Structure Determination, X-ray Diffraction for • Ultrafast Diffraction Techniques

REFERENCES

1. E.W.G. Diau, S. DeFeyter, A.H. Zewail, 'Femtosecond Dynamics of Retro Diels–Alder Reactions: The Concept of Concertedness', *Chem. Phys. Lett.*, **304**(3–4), 134–144 (1999).
2. G. Porter, 'Flash Photolysis', *Proc. R. Soc. London, Ser. A*, **200**, 284–300 (1950).
3. H.W. Mocker, R.J. Collins, 'Mode locked Ruby Laser', *Appl. Phys. Lett.*, **7**, 270–273 (1965).
4. A.J. DeMaria, D.A. Stetser, H. Heynau, 'Mode locked Nd Glass', *Appl. Phys. Lett.*, **8**, 174–176 (1966).
5. M.P. Irvine, R.J. Harrison, G.S. Beddard, P. Leighton, J.K.M. Sanders, 'Detection of the Inverted Region in the Photoinduced Intramolecular Electron Transfer of Capped Porphyrins', *Chem. Phys.*, **104**(2), 315–324 (1986).
6. J.R. Miller, J.V. Beitz, R.K. Huddleston, 'Effect of Free Energy on Rates of Electron Transfer Between Molecules', *J. Am. Chem. Soc.*, **106**(18), 5057–5068 (1984).
7. R.A. Marcus, 'ET', *J. Chem. Phys.*, **24**, 966–978 (1956).
8. R.M. Bowman, K.B. Eisenthal, D.P. Millar, 'Frictional Effects on Barrier Crossing in Solution – Comparison with the Kramers Equation', *J. Chem. Phys.*, **89**(2), 762–769 (1988).
9. M.G. Hyde, G.S. Beddard, 'Picosecond Photodissociation and Geminate Radical Recombination in Alkane Solutions of Tetraphenylhydrazine', *Chem. Phys.*, **151**(2), 239–248 (1991).
10. R.L. Fork, B.I. Greene, C.V. Shank, 'First CPM', *Appl. Phys. Lett.*, **38**(9), 671–672 (1981).
11. J.A. Valdmanis, R.L. Fork, 'prism CPM', *IEEE J. Quantum Electron.*, **22**, 112–118 (1986).
12. R.L. Fork, C.V. Shank, R.T. Yen, '10 Hz Amp', *Appl. Phys. Lett.*, **41**(3), 223–225 (1982).
13. A. Zewail, *The Chemical Bond. Structure and Dynamics*, Academic Press, Boston, 1992.
14. R.L. Fork, C. Brito, C.H.P.C. Becker, C.V. Shank, 'Compression of Optical Pulses to Six Femtoseconds by Using Cubic Phase Compensation', *Opt. Lett.*, **12**, 483–485 (1987).
15. D.E. Spence, P.N. Kean, W. Sibbett, '60-fs Pulse Generation From a Self-mode-locked Ti–Sapphire Laser', *Opt. Lett.*, **16**(1), 42–44 (1991).
16. D. Strickland, G. Mourou, 'Compression of Amplified Chirped Optical Pulses', *Opt. Commun.*, **55**(6), 447–449 (1985).
17. T. Elsaesser, J.G. Fujimoto, D.A. Wiersma, W. Zinth (eds.), *Ultrafast Phenomena XI (formerly Picosecond Phenomena)*, Springer, Berlin, Vol. 63, 1998.
18. A.E. Siegman, *Lasers*, University Science Books, Mill Valley, CA, 1986.
19. O. Svelto, *Principles of Lasers*, 3rd edition, Plenum Press, New York, 1989.
20. J.D. Simon, 'Ultrashort Light Pulses', *Rev. Sci. Instrum.*, **60**(12), 3597–3624 (1989).
21. P.F. Moulton, 'Spectroscopic and Laser Characteristics of $TiAl_2O_3$', *J. Opt. Soc. Am. B*, **3**(1), 125–133 (1986).
22. M.T. Asaki, C.P. Huang, D. Garvey, J.P. Zhou, H.C. Kapteyn, M.M. Murnane, 'Generation of 11-fs Pulses from a Self-mode-locked Ti–Sapphire Laser', *Opt. Lett.*, **18**(12), 977–979 (1993).
23. I.P. Christov, V.D. Stoev, M.M. Murnane, H.C. Kapteyn, 'Sub-10-fs Operation of Kerr-lens Mode-locked Lasers', *Opt. Lett.*, **21**(18), 1493–1495 (1996).
24. M.S. Pshenichnikov, W.P. Deboeij, D.A. Wiersma, 'Generation of 13-fs, 5-MW Pulses from a Cavity-dumped Ti–Sapphire Laser', *Opt. Lett.*, **19**(8), 572–574 (1994).

25. A. Stingl, C. Spielmann, F. Krausz, R. Szipocs, 'Generation of 11-fs Pulses from a Ti–Sapphire Laser without the Use of Prisms', *Opt. Lett.*, **19**(3), 204–206 (1994).
26. U. Morgner, F.X. Kartner, S.H. Cho, Y. Chen, H.A. Haus, J.G. Fujimoto, E.P. Ippen, V. Scheuer, G. Angelow, T. Tschudi, 'Sub-two-cycle Pulses from a Kerr-lens Mode-locked Ti:Sapphire Laser', *Opt. Lett.*, **24**(6), 411–413 (1999).
27. I.D. Jung, F.X. Kartner, N. Matuschek, D.H. Sutter, F. Morier-Genoud, G. Zhang, U. Keller, V. Scheuer, M. Tilsch, T. Tschudi, 'Self-starting 6.5-fs Pulses from a Ti:Sapphire Laser', *Opt. Lett.*, **22**(13), 1009–1011 (1997).
28. M.A. Arbore, M.M. Fejer, M.E. Fermann, A. Hariharan, A. Galvanauskas, D. Harter, 'Frequency Doubling of Femtosecond Erbium-fiber Soliton Lasers in Periodically Poled Lithium Niobate', *Opt. Lett.*, **22**(1), 13–15 (1997).
29. S. Backus, C.G. Durfee, M.M. Murnane, H.C. Kapteyn, 'High Power Ultrafast Lasers', *Rev. Sci. Instrum.*, **69**(3), 1207–1223 (1998).
30. R.L. Fork, O.E. Martinez, J.P. Gordon, 'Prism Compression', *Opt. Lett.*, **9**, 150–152 (1984).
31. E.B. Treacy, 'Optical Pulse Compression with Diffraction Gratings', *IEEE J. Quantum Electron.*, **5**(9), 454–458 (1969).
32. O.E. Martinez, '3000 Times Grating Compressor with Positive Group-velocity Dispersion – Application to Fiber Compensation in 1.3–1.6 μm Region', *IEEE J. Quantum Electron.*, **23**(1), 59–64 (1987).
33. G. Cheriaux, P. Rousseau, F. Salin, J.P. Chambaret, B. Walker, L.F. Dimauro, 'Aberration-free Stretcher Design for Ultrashort-pulse Amplification', *Opt. Lett.*, **21**(6), 414–416 (1996).
34. J.V. Rudd, G. Korn, S. Kane, J. Squier, G. Mourou, P. Bado, 'Chirped-pulse Amplification of 55-fs Pulses at a 1-kHz Repetition Rate in a Ti–Al_2O_3 Regenerative Amplifier', *Opt. Lett.*, **18**(23), 2044–2046 (1993).
35. C.P.J. Barty, C.L. Gordon, B.E. Lemoff, 'Multiterawatt 30-fs Ti–Sapphire Laser System', *Opt. Lett.*, **19**(18), 1442–1444 (1994).
36. S. Backus, J. Peatross, C.P. Huang, M.M. Murnane, H.C. Kapteyn, 'Ti–Sapphire Amplifier Producing Millijoule-level, 21-fs Pulses at 1 kHz', *Opt. Lett.*, **20**(19), 2000–2002 (1995).
37. J.P. Chambaret, C. LeBlanc, G. Cheriaux, P. Curley, G. Darpentigny, P. Rousseau, G. Hamoniaux, A. Antonetti, F. Salin, 'Generation of 25-TW, 32-fs Pulses at 10 Hz', *Opt. Lett.*, **21**(23), 1921–1923 (1996).
38. S. Backus, C.G. Durfee, M.M. Murnane, H.C. Kapteyn, 'High Power Ultrafast Lasers', *Rev. Sci. Instrum.*, **69**(3), 1207–1223 (1998).
39. S. Backus, C.G. Durfee, G. Mourou, H.C. Kapteyn, M.M. Murnane, '0.2-TW Laser System at 1 kHz', *Opt. Lett.*, **22**(16), 1256–1258 (1997).
40. F. Salin, C. LeBlanc, J. Squier, C. Barty, 'Thermal Eigenmode Amplifiers for Diffraction-limited Amplification of Ultrashort Pulses', *Opt. Lett.*, **23**(9), 718–720 (1998).
41. K. Wynne, G.D. Reid, R.M. Hochstrasser, 'Regenerative Amplification of 30-fs Pulses in Ti–Sapphire at 5 kHz', *Opt. Lett.*, **19**(12), 895–897 (1994).
42. J. Squier, C.P.J. Barty, F. Salin, C. LeBlanc, S. Kane, 'Use of Mismatched Grating Pairs in Chirped-pulse Amplification Systems', *Appl. Opt.*, **37**(9), 1638–1641 (1998).
43. G.D. Reid, 'Use of Mismatched Gratings in Conjunction with High Dispersion Prism Pairs in Chirped-pulse Amplification Systems', in preparation.
44. C.P.J. Barty, T. Guo, C. LeBlanc, F. Raksi, C. RosePetruck, J. Squier, K.R. Wilson, V.V. Yakovlev, K. Yamakawa, 'Generation of 18-fs, Multiterawatt Pulses by Regenerative Pulse Shaping and Chirped-pulse Amplification', *Opt. Lett.*, **21**(9), 668–670 (1996).
45. L. Dhar, J.A. Rogers, K.A. Nelson, 'Time-resolved Vibrational Spectroscopy in the Impulsive Limit', *Chem. Rev.*, **94**(1), 157–193 (1994).
46. W.H. Knox, R.L. Fork, M.C. Downer, R.H. Stolen, C.V. Shank, J.A. Valdmanis, 'Optical Pulse Compression to 8 fs at a 5-kHz Repetition Rate', *Appl. Phys. Lett.*, **46**(2), 1120–1121 (1985).
47. M. Nisoli, S. Stagira, S. DeSilvestri, O. Svelto, S. Sartania, Z. Cheng, M. Lenzner, C. Spielmann, F. Krausz, 'A Novel High Energy Pulse Compression System: Generation of Multigigawatt Sub-5-fs Pulses', *Appl. Phys. B*, **65**(2), 189–196 (1997).
48. A.M. Weiner, 'Effect of Group Velocity Mismatch on the Measurement of Ultrashort Optical Pulses via Second Harmonic Generation', *IEEE J. Quantum Electron.*, **19**(8), 1276–1283 (1983).
49. J. Ringling, O. Kittelmann, F. Noack, G. Korn, J. Squier, 'Tunable Femtosecond Pulses in the Near Vacuum Ultraviolet Generated by Frequency Conversion of Amplified Ti–Sapphire Laser Pulses', *Opt. Lett.*, **18**(23), 2035–2037 (1993).
50. A. Rundquist, C.G. Durfee, Z.H. Chang, C. Herne, S. Backus, M.M. Murnane, H.C. Kapteyn, 'Phase-matched Generation of Coherent Soft X-rays', *Science*, **280**(5368), 1412–1415 (1998).
51. C.G. Durfee, S. Backus, H.C. Kapteyn, M.M. Murnane, 'Intense 8-fs Pulse Generation in the Deep Ultraviolet', *Opt. Lett.*, **24**(10), 697–699 (1999).
52. M. Lenzner, M. Schnuerer, C. Spielmann, F. Krausz, 'Extreme Nonlinear Optics with Few-cycle Laser Pulses', *IEICE Trans. Electron.*, **E81-C**(2), 112–122 (1998).
53. J. Wark, 'Time-resolved X-ray Diffraction', *Contemp. Phys.*, **37**(3), 205–218 (1996).
54. D. Giulieti, L.A. Gizzi, 'X-ray Emission from Laser-produced Plasmas', *Riv. Nuovo Cimento*, **21**(10), 1–93 (1998).
55. R.W. Schoenlein, W.P. Leemans, A.H. Chin, P. Volfbeyn, T.E. Glover, P. Balling, M. Zolotorev, K.J. Kim, S. Chattopadhyay, C.V. Shank, 'Femtosecond X-ray Pulses at 0.4 Ångstrom Generated by 90 Degrees Thomson Scattering: A Tool for Probing the Structural

Dynamics of Materials', *Science*, **274**(5285), 236–238 (1996).
56. Y.R. Shen, *The Principles of Nonlinear Optics*, Wiley, New York, 1986.
57. B. Akhremitchev, C.F. Wang, G.C. Walker, 'A Femtosecond Absorption Spectrometer Tunable from 50 000 to 800 cm^{-1}: Nonlinear Optics and Pump/Probe Geometries', *Rev. Sci. Instrum.*, **67**(11), 3799–3805 (1996).
58. D.T. Reid, G.T. Kennedy, A. Miller, M. Sibbett, M. Ebrahimzadeh, 'Widely Tunable, Near- to Mid-infrared Femtosecond and Picosecond Optical Parametric Oscillators Using Periodically Poled $LiNbO_3$ and $RbTiOAsO_4$', *IEEE J. Sel. Top. Quantum Electron.*, **4**(2), 238–248 (1998).
59. P. Hamm, S. Wiemann, M. Zurek, W. Zinth, 'Highly Sensitive Multichannel Spectrometer for Subpicosecond Spectroscopy in the Midinfrared', *Opt. Lett.*, **19**(20), 1642–1644 (1994).
60. K. Wynne, R.M. Hochstrasser, 'The Theory of Ultrafast Vibrational Spectroscopy', *Chem. Phys.*, **193**(3), 211–236 (1995).
61. T. Wilhelm, J. Piel, E. Riedle, 'Sub-20-fs Pulses Tunable Across the Visible from a Blue-pumped Single-pass Noncollinear Parametric Converter', *Opt. Lett.*, **22**(19), 1494–1496 (1997).
62. A. Shirakawa, I. Sakane, M. Takasaka, T. Kobayashi, 'Sub-5-fs Visible Pulse Generation by Pulse-front-matched Noncollinear Optical Parametric Amplification', *Appl. Phys. Lett.*, **74**(16), 2268–2270 (1999).
63. P.R. Smith, D.H. Auston, M.C. Nuss, 'Subpicosecond Photoconducting Dipole Antennas', *IEEE J. Quantum Electron.*, **24**(2), 255–260 (1988).
64. D. Grischkowsky, S. Keiding, M. van Exter, C. Fattinger, 'Far-infrared Time-domain Spectroscopy with Terahertz Beams of Dielectrics and Semiconductors', *J. Opt. Soc. Am. B*, **7**, 2006–2015 (1990).
65. D. You, R.R. Jones, P.H. Bucksbaum, D.R. Dykaar, 'Generation of High-power Sub-single-cycle 500-fs Electromagnetic Pulses', *Opt. Lett.*, **18**(4), 290–292 (1993).
66. A. Nahata, A.S. Weling, T.F. Heinz, 'A Wideband Coherent Terahertz Spectroscopy System Using Optical Rectification and Electro-optic Sampling', *Appl. Phys. Lett.*, **69**(16), 2321–2323 (1996).
67. Q. Wu, X.-C. Zhang, '7 Terahertz Broadband GaP Electro-optic Sensor', *Appl. Phys. Lett.*, **70**(14), 1784–1786 (1997).
68. Q. Wu, X.-C. Zhang, 'Ultrafast Electro-optic Field Sensors', *Appl. Phys. Lett.*, **68**(12), 1604–1606 (1996).
69. Z. Jiang, X.-C. Zhang, 'Electro-optic Measurement of THz Field Pulses with a Chirped Optical Beam', *Appl. Phys. Lett.*, **72**(16), 1945–1947 (1998).
70. A. Leitenstorfer, S. Hunsche, J. Shah, M.C. Nuss, W.H. Knox, 'Detectors and Sources for Ultrabroadband Electro-optic Sampling: Experiment and Theory', *Appl. Phys. Lett.*, **74**(11), 1516–1518 (1999).
71. G. Mourou, S. Williamson, 'Picosecond Electron Diffraction', *Appl. Phys. Lett.*, **41**(1), 44–45 (1982).
72. H.E. Elsayed-Ali, J.W. Herman, 'Ultrahigh Vacuum Picosecond Laser-driven Electron Diffraction System', *Rev. Sci. Instrum.*, **61**(6), 1636–1647 (1990).
73. V.A. Lobastov, J.D. Ewbank, L. Schaefer, A.A. Ischenko, 'Instrumentation for Time-resolved Electron Diffraction Spanning the Time Domain from Microseconds to Picoseconds', *Rev. Sci. Instrum.*, **69**(7), 2633–2643 (1998).
74. M. Dantus, S.B. Kim, J.C. Williamson, A.H. Zewail, 'Ultrafast Electron Diffraction. 5. Experimental Time Resolution and Applications', *J. Phys. Chem.*, **98**, 2782–2796 (1994).
75. D.T. Reid, W. Sibbett, J.M. Dudley, L.P. Barry, B. Thomsen, J.D. Harvey, 'Commercial Semiconductor Devices for Two Photon Absorption Autocorrelation of Ultrashort Light Pulses', *Appl. Opt.*, **37**(34), 8142–8144 (1998).
76. K.L. Sala, G.A. Kenney-Wallace, G.E. Hall, 'CW Autocorrelation Measurements of Picosecond Laser Pulses', *IEEE J. Quantum Electron.*, **16**(9), 990–996 (1980).
77. K. Naganuma, K. Mogi, H. Yamada, 'General Method for Ultrashort Light-pulse Chirp Measurement', *IEEE J. Quantum Electron.*, **25**(6), 1225–1233 (1989).
78. K.W. DeLong, D.N. Fittinghoff, R. Trebino, 'Practical Issues in Ultrashort-laser-pulse Measurement Using Frequency-resolved Optical Gating', *IEEE J. Quantum Electron.*, **32**(7), 1253–1264 (1996).
79. R. Trebino, D.J. Kane, 'Using Phase Retrieval to Measure the Intensity and Phase of Ultrashort Pulses – Frequency-resolved Optical Gating', *J. Opt. Soc. Am. A*, **10**(5), 1101–1111 (1993).
80. K.W. Delong, C.L. Ladera, R. Trebino, B. Kohler, K.R. Wilson, 'Ultrashort-pulse Measurement Using Noninstantaneous Nonlinearities – Raman Effects in Frequency-resolved Optical Gating', *Opt. Lett.*, **20**(5), 486–488 (1995).
81. G. Nunes, M.R. Freeman, 'Picosecond Resolution in Scanning-tunneling-microscopy', *Science*, **262**(5136), 1029–1032 (1993).
82. D. Botkin, J. Glass, D.S. Chemla, D.F. Ogletree, M. Salmeron, S. Weiss, 'Advances in Ultrafast Scanning Tunneling Microscopy', *Appl. Phys. Lett.*, **69**(9), 1321–1323 (1996).
83. G.M. Steeves, A.Y. Elezzabi, M.R. Freeman, 'Nanometer-scale Imaging with an Ultrafast Scanning Tunneling Microscope', *Appl. Phys. Lett.*, **72**(4), 504–506 (1998).
84. M.J. Feldstein, P. Vöhringer, W. Wang, N.F. Scherer, 'Femtosecond Optical Spectroscopy and Scanning Probe Microscopy', *J. Phys. Chem.*, **100**, 4739–4748 (1996).
85. N.F. Scherer, R.J. Carlson, A. Matro, M. Du, A.J. Ruggiero, V. Romero-Rochin, J.A. Cina, G.R. Fleming, S.A. Rice, 'Fluorescence-detected Wave Packet Interferometry: Time Resolved Molecular Spectroscopy with

Sequences of Femtosecond Phase-locked Pulses', *J. Chem. Phys.*, **95**(3), 1487–1511 (1991).
86. M.J. Rosker, T.S. Rose, A.H. Zewail, 'Femtosecond Real-time Dynamics of Photofragment-trapping Resonances on Dissociative Potential Energy Surfaces', *Chem. Phys. Lett.*, **146**(3,4), 175–179 (1988).
87. G.A. Voth, R.M. Hochstrasser, 'Transition State Dynamics and Relaxation Processes in Solutions: A Frontier of Physical Chemistry', *J. Phys. Chem.*, **100**(31), 13034–13049 (1996).
88. N. Pugliano, A.Z. Szarka, R.M. Hochstrasser, 'Relaxation of the Product State Coherence Generated Through the Photolysis of HgI_2 in Solution', *J. Chem. Phys.*, **104**(13), 5062–5079 (1996).
89. Y. Yan, R.M. Whitnell, K.R. Wilson, A.H. Zewail, 'Femtosecond Chemical Dynamics in Solution. Wavepacket Evolution and Caging of I_2', *Chem. Phys. Lett.*, **193**(5), 402–412 (1992).
90. N.F. Scherer, L.D. Ziegler, G.R. Fleming, 'Heterodyne-detected Time-domain Measurement of I_2 Predissociation and Vibrational Dynamics in Solution', *J. Chem. Phys.*, **96**, 5544–5547 (1992).
91. K. Wynne, R.M. Hochstrasser, 'Coherence and Adiabaticity in Ultrafast Electron Transfer', *Adv. Chem. Phys.*, **107**, 263–309 (1999).
92. R.M. Williams, J.B. Shear, W.R. Zipfel, S. Maiti, W.W. Webb, 'Mucosal Mast Cell Secretion Processes Imaged Using Three-photon Microscopy of 5-Hydroxytryptamine Autofluorescence', *Biophys. J.*, **76**(4), 1835–1846 (1999).
93. T.Y.F. Tsang, 'Optical 3rd-harmonic Generation at Interfaces', *Phys. Rev. A*, **52**(5), 4116–4125 (1995).
94. Y. Barad, H. Eisenberg, M. Horowitz, Y. Silberberg, 'Nonlinear Scanning Laser Microscopy by Third Harmonic Generation', *Appl. Phys. Lett.*, **70**(8), 922–924 (1997).
95. J.A. Squier, M. Muller, G.J. Brakenhoff, K.R. Wilson, 'Third Harmonic Generation Microscopy', *Opt. Express*, **3**(9), 315–324 (1998).
96. D.N. Fittinghoff, A.C. Millard, J.A. Squier, M. Muller, 'Frequency-resolved Optical Gating Measurement of Ultrashort Pulses Passing Through a High Numerical Aperture Objective', *IEEE J. Quantum Electron.*, **35**(4), 479–486 (1999).
97. A.C. Millard, D.N. Fittinghoff, J.A. Squier, M. Muller, A.L. Gaeta, 'Using GaAsP Photodiodes to Characterize Ultrashort Pulses Under High Numerical Aperture Focusing in Microscopy', *J. Microsc.*, **193**(Pt. 3), 179–181 (1999).
98. J.A. Squier, D.N. Fittinghoff, C.P.J. Barty, K.R. Wilson, M. Muller, G.J. Brakenhoff, 'Characterization of Femtosecond Pulses Focused with High Numerical Aperture Optics Using Interferometric Surface-third-harmonic Generation', *Opt. Commun.*, **147**(1–3), 153–156 (1998).
99. K. Wynne, D.A. Jaroszynski, 'Superluminal Terahertz Pulses', *Opt. Lett.*, **24**(1), 25–27 (1999).
100. D.M. Mittleman, R.H. Jacobsen, M.C. Nuss, 'T-ray Imaging', *IEEE J. Sel. Top. Quantum Electron.*, **2**(3), 679–692 (1996).
101. D.M. Mittleman, M. Gupta, R. Neelamani, R.G. Baraniuk, J.V. Rudd, M. Koch, 'Recent Advances in Terahertz Imaging', *Appl. Phys. B*, **68**(6), 1085–1094 (1999).
102. S. Hunsche, M. Koch, I. Brener, M.C. Nuss, 'THz Near-field Imaging', *Opt. Commun.*, **150**(1–6), 22–26 (1998).
103. Q. Wu, T.D. Hewitt, X.-C. Zhang, 'Two-dimensional Electro-optic Imaging of THz Beams', *Appl. Phys. Lett.*, **69**(8), 1026–1028 (1996).
104. G.J. Tearney, B.E. Bouma, S.A. Boppart, B. Golubovic, E.A. Swanson, J.G. Fujimoto, 'Rapid Acquisition of in Vivo Biological Images by Use of Optical Coherence Tomography', *Opt. Lett.*, **21**(17), 1408–1410 (1996).
105. N. Grigorieff, T.A. Ceska, K.H. Downing, J.M. Baldwin, R. Henderson, 'Electron-crystallographic Refinement of the Structure of Bacteriorhodopsin', *J. Mol. Biol.*, **259**, 393–421 (1996).
106. R. Henderson, 'The Potential and Limitations of Neutrons, Electrons and X-rays for Atomic Resolution Microscopy of Unstained Biological Molecules', *Q. Rev. Biophys.*, **28**(2), 171–193 (1995).
107. B.L. Stoddard, 'New Results Using Laue Diffraction and Time-resolved Crystallography', *Curr. Opin. Struct. Biol.*, **8**, 612–618 (1998).
108. K. Moffat, 'Ultrafast Time-resolved Crystallography', *Nature Struct. Biol.*, **5**, 641–643 (1998).
109. H. Ihee, J. Cao, A.H. Zewail, 'Ultrafast Electron Diffraction: Structures in Dissociation Dynamics of $Fe(CO)_5$', *Chem. Phys. Lett.*, **281**, 10–19 (1997).
110. J. Cao, H. Ihee, A.H. Zewail, 'Ultrafast Electron Diffraction and Direct Observation of Transient Structures in a Chemical Reaction', *Proc. Natl. Acad. Sci. USA*, **96**, 338–342 (1999).
111. A.H. Chin, R.W. Schoenlein, T.E. Glover, P. Balling, W.P. Leemans, C.V. Shank, 'Ultrafast Structural Dynamics in InSb Probed by Time-resolved X-ray Diffraction', *Phys. Rev. Lett.*, **83**(2), 336–339 (1999).
112. C. Rose-Petruck, R. Jimenez, T. Guo, A. Cavalleri, C.W. Siders, F. Raksi, J.A. Squier, B.C. Walker, K.R. Wilson, C.P.J. Barty, 'Picosecond-milliangstrom Lattice Dynamics Measured by Ultrafast X-ray Diffraction', *Nature (London)*, **398**(6725), 310–312 (1999).